Pure and Applied Geophysics

Geophysical Investigation of Mount Nemrut Stratovolcano (Bitlis, Eastern Turkey) Through Aeromagnetic Anomaly Analyses

Yunus Levent Ekİncİ,[1,2] Aydin Büyüksaraç,[3] Özcan Bektaş,[4] and Can Ertekİn[5,6]

Abstract—Quaternary Mount Nemrut stratovolcano, having a spectacular summit caldera and associated lakes, is located north of the Bitlis–Zagros suture zone, Eastern Turkey. Although much attention has been paid to its geology, morphology, history and biology, a detailed geophysical investigation has not been performed in this special region. Thus, we attempted to characterize the stratovolcano and the surroundings using total field aeromagnetic anomalies. Potential field data processing techniques helped us to interpret geologic sources causing magnetic signatures. Resulting image maps obtained from some linear transformations and a derivative-based technique revealed general compatibility between the aeromagnetic anomalies and the near-surface geology of the study area. Some high amplitude magnetic anomalies observed north of the Nemrut caldera rim are associated with the latest bimodal volcanic activity marked by lava fountains and comenditic-basaltic flows occurred along the rift zone. After minimizing the high-frequency effects, a pseudogravity-based three-dimensional inversion scheme revealed that the shallowest deep-seated sources are located about 3.0 km below the ground surface. Two-dimensional normalized full gradient solutions also exposed the depths of these anomaly sources, in good agreement with the inversion results. This first geophysical study performed through aeromagnetic anomalies clearly gave insights into some main magnetized structures of the Mount Nemrut stratovolcano.

Keywords: Bitlis, Mount Nemrut stratovolcano, aeromagnetic anomalies, linear transformations, inversion, normalized full gradient.

[1] Department of Archaeology, Bitlis Eren University, TR-13100 Bitlis, Turkey. E-mail: ylekinci@beu.edu.tr

[2] Career Application and Research Center, Bitlis Eren University, TR-13100 Bitlis, Turkey.

[3] Çan Vocational School, Çanakkale Onsekiz Mart University, TR-17400 Çan/Çanakkale, Turkey.

[4] Department of Geophysical Engineering, Sivas Cumhuriyet University, TR-58140 Sivas, Turkey.

[5] Aegean Regional Directorate of Mineral Research and Exploration, TR-35040 İzmir, Turkey.

[6] Graduate School of Natural and Applied Sciences, Department of Geological Engineering, Çanakkale Onsekiz Mart University, TR-17020 Çanakkale, Turkey.

1. Introduction

Magnetic prospection can be performed for the investigation of the geological structures, limited between the surface and Curie temperature isotherm due to the well-known rock magnetism of the crust (Blakely 1988; Xu et al. 2011; Bektaş et al. 2007; Aydemir 2009; Ekinci and Yiğitbaş 2012; Balkaya et al. 2012, 2017; Boukerbout et al. 2018). The method is suitable for numerous applications ranging from shallow site investigations through to large-scale ones such as hydrocarbon explorations (Reynolds 1997). The magnetic features of the rocks are related to magnetic minerals such as Fe-Oxides. Generally, basic igneous rocks resulted from the solidifications of magma have the highest magnetic susceptibilities and therefore they produce high amplitude anomalies in comparison to other rock types (Sharma 1986; Telford et al. 1990; Kearey et al. 2002). Bulk rock composition, oxidation rate, hydrothermal alteration, and metamorphism affect the magnetic properties of igneous rocks (Hinze et al. 2013). The magnetic anomalies of a volcanic region can give insights into the structural and volcanological properties of the region. There have been many studies about the volcanic areas using magnetic anomalies so far (e.g. Fedi et al. 1998; Patella and Mauriello 1999; Secomandi et al. 2003; Büyüksaraç et al. 2005; Zurek and Williams-Jones 2013; Longo et al. 2016; Afshar et al. 2017; Bilim et al. 2017; Paoletti et al. 2017; Nicolosi et al. 2019; Sawires and Aboud 2019).

Turkey is located in an actively deforming region (Bozkurt 2001) and volcanism contributed to the geological evolution of the country. This volcanism

originated from the collision between Arabian and Anatolian plates (Yılmaz et al. 1987, 1998; Şen et al. 2004; Karaoğlu et al. 2005; Özdemir et al. 2006) remarkably affected the geomorphology of eastern Turkey (Ulusoy et al. 2008). In this region, the known youngest volcanic center is the Mount Nemrut which has three evolutionary stages (Aydar et al. 2003; Özdemir et al. 2006; Çubukçu 2008; Ulusoy 2008). These stages are pre-caldera extending from 1.01 ± 0.04 Ma to 80 ± 20 ka, syn-caldera between at least 89 ka and fewer ages as 30 ka, and post-caldera extending from 30 ka to the historical times. Basaltic lavas of the main cone and twenty craters of various sizes, ranging from 10 to 100 m in diameter are the clues showing that Mount Nemrut is a stratovolcano structure (Yılmaz et al. 1998). Mount Nemrut stratovolcano having a spectacular elliptical summit caldera with 8.5×7 km diameter (Ulusoy et al. 2008) is a polygenetic stratovolcano (Yılmaz et al. 1998). The caldera is also a natural relic since 2003 (Seven et al. 2019). In the caldera, there are two permanent lakes (Nemrut and Hot Lakes) covering an area of 12.83 km^2 and three seasonal small lakes. Ten pyroclastic deposits of maar, 12 lava domes, and 3 lava flows fill the other parts of the caldera. (Ulusoy et al. 2008). Nemrut was considered a dormant volcano before (Yılmaz et al. 1998). However, data obtained from the first seismic network for volcano monitoring in Turkey revealed 33 volcanic-linked seismic events (Ulusoy 2008). Thus, we can say that the Nemrut stratovolcano is quiescent. Pre-caldera products are mainly lava flows and domes. Pyroclastic series indicate the syn-caldera stage, of which sequences consist of plinian units and ignimbrite flows. Post-caldera activity is represented by basaltic-rhyolitic effusive activity, even in historical times (Karakhanian et al. 2002; Ulusoy 2008) and hydrothermal activity in the caldera and on the Nemrut rift zone (Ulusoy et al. 2008). The volcanic rocks from basalt to rhyolite and pyroclastics spread over a large plateau of the Miocene continents (Yılmaz et al. 1998). Although Mount Nemrut stratovolcano has been extendedly studied, a comprehensive geophysical characterization is still lacking. Hence, we analyzed the total field aeromagnetic anomalies of this region for the first time. We used linear transformations (Reduction-to-the-

pole (RTP), pseudogravity transformation (PSG), upward continuation), total horizontal derivative (THD), radially averaged power spectrum, a statistical approach, three-dimensional inversion and two-dimensional normalized full gradient (NFG) to better understand the surface and subsurface sources causing magnetic anomalies.

2. Tectonic Setting and Geology

Subduction and collision events were mainly following the closure of Paleo-Tethys during the Middle Jurassic. The onset of subduction was the Late Jurassic (?)-Early Cretaceous in the south of Pontides in Fig. 1 (Şengör and Yılmaz 1981; Kuzucuoğlu et al. 2019). Through the Middle Cretaceous, another subduction zone initiated to act. Both subduction zones eliminated as a part of Neo-Tethys, the line of which lies along İzmir-Ankara-Erzincan (Fig. 1) and ended with collisions during the Middle Eocene (Kuzucuoğlu et al. 2019). Following the collision, the shortening or squeezing continued in Early Miocene (Burdigalian) into the west of the Eastern Anatolia Plateau (NE Anatolian Plate in Fig. 1) and, in the Late Paleocene in the west of Anatolia. During the Early Miocene (Burdigalian, ca. 20 Ma ago), the different collision commenced in southeastern Anatolia caused by the Arabian Plate sliding under the Anatolian Plate (Koçyiğit et al. 2001; Kuzucuoğlu et al. 2019). In contrast, the southern branch of Neo-Tethys (known as the Bitlis Ocean) persisted in the Middle Miocene (Serravalian, ca. 11–13 Ma ago) and then closed completely by continent–continent collision and suturing. The suture is known as Bitlis–Zagros Suture (Fig. 1). The collision N–S directed and following the post-collisional intracontinental convergence continued at the end of Late Miocene and Early Pliocene (Koçyiğit et al. 2001). The region (Eastern Anatolia Plateau in the present) intervened both of Lesser Caucasus (Fig. 1) and Bitlis–Zagros Suture began rising ($\sim$ 2 km-high plateau in the present) while the west of Anatolia was under the extension regime (Kuzucuoğlu et al. 2019). The rising let form Anatolian Plate, dextral (right sided) North Anatolian Fault Zone and sinistral (left sided) East Anatolian Fault
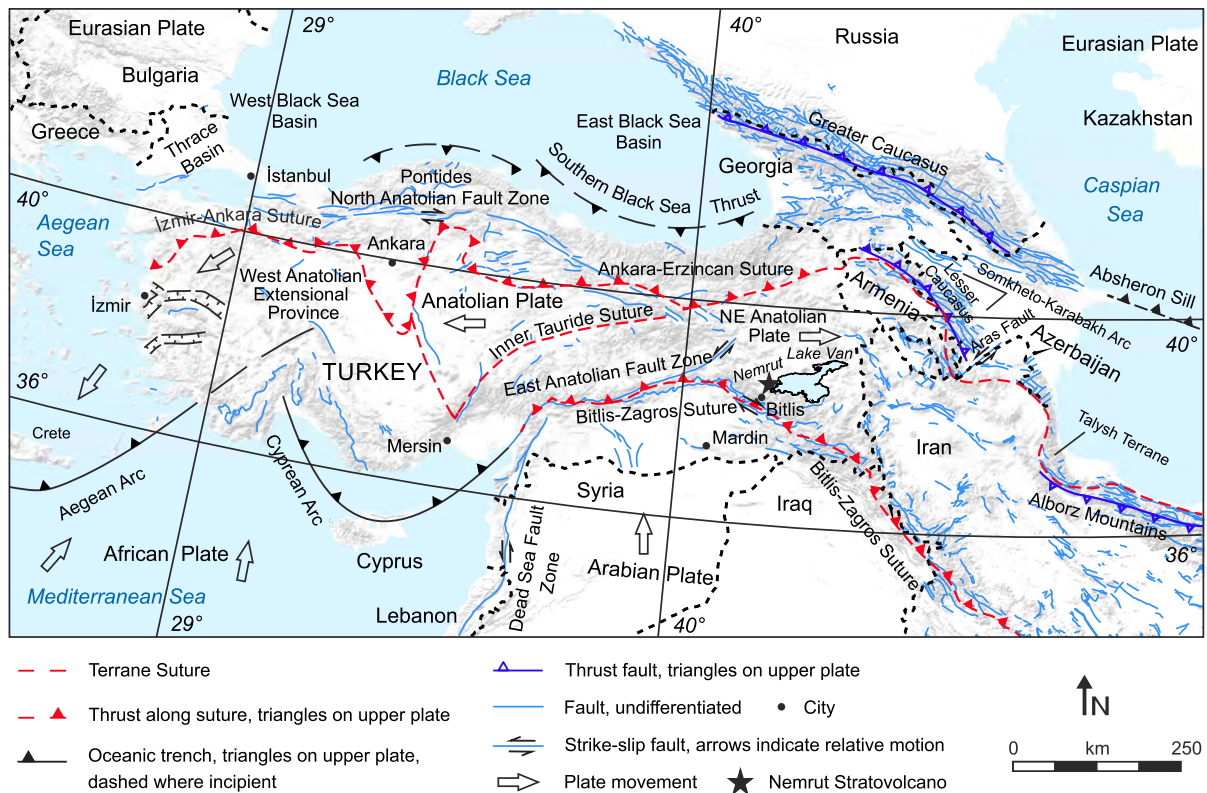
Figure 1

Simplified neotectonic map showing major sutures, faults, and geologic and geographic features in Turkey and the surrounding area (modified from Okay and Tüysüz 1999; USGS 2010; Yiğitbaş et al. 2004; Ekinci et al. 2013; Ekinci and Yiğitbaş 2012, 2015)

Zone (Fig. 1) (Şengör et al. 1985). The forming of the two fault zones provoked WSW direction escape of Anatolian Plate (plate movements in Fig. 1) from the convergent zone onto the oceanic lithosphere of the African Plate (Koçyiğit et al. 2001; Kuzucuoğlu et al. 2019). The post-collisional condition is also responsible for magmatism (Şengör et al. 2008) and its surface expression as volcanism. The volcanic activity of Eastern Anatolia Plateau increased during the late Miocene–Pliocene, continued during Quaternary and even in historical times (Yılmaz et al. 1998). The ages of the volcanic rocks vary from about 11 Ma to possibly seventeenth century A.D. and they are derived from an enriched mantle (Şengör et al. 2008).

The tectonic regime initiated the formation of Nemrut, Süphan and Ağrı stratovolcanoes, and Tendürek shield volcano (Karaoğlu et al. 2005, 2017) in Eastern Turkey (Fig. 2). The first volcanic manifestation in Nemrut initiated with metaluminous trachytic lavas (Ulusoy et al. 2019). The development of the main cone was associated with events of peralkaline rocks (comendites, pantellerites) and comenditic trachytes (Çubukçu 2008). Peripheral silicic doming characterizes the pre-caldera stage. Mazik and Kirkor Dome Complexes are the largest silicic ones placed southwest and western side of Nemrut volcano (Fig. 3). During this stage, basaltic trachyandesitic (mugearite) lava flows formed and outcrop the southern and southwestern flanks on the recent topography (Fig. 3). Explosive eruptions occurred during syn-caldera stage of the volcano evolution (Ulusoy et al. 2019) and produced pyroclastic fall/flow deposits known as Nemrut and Kantaşı ignimbrites (Ulusoy et al. 2012). Post-caldera rocks exist in the caldera and on the Nemrut rift zone (Fig. 3). Rhyolite (comendite) rocks partly cover the inner-caldera surface. The fissure eruption on the rift
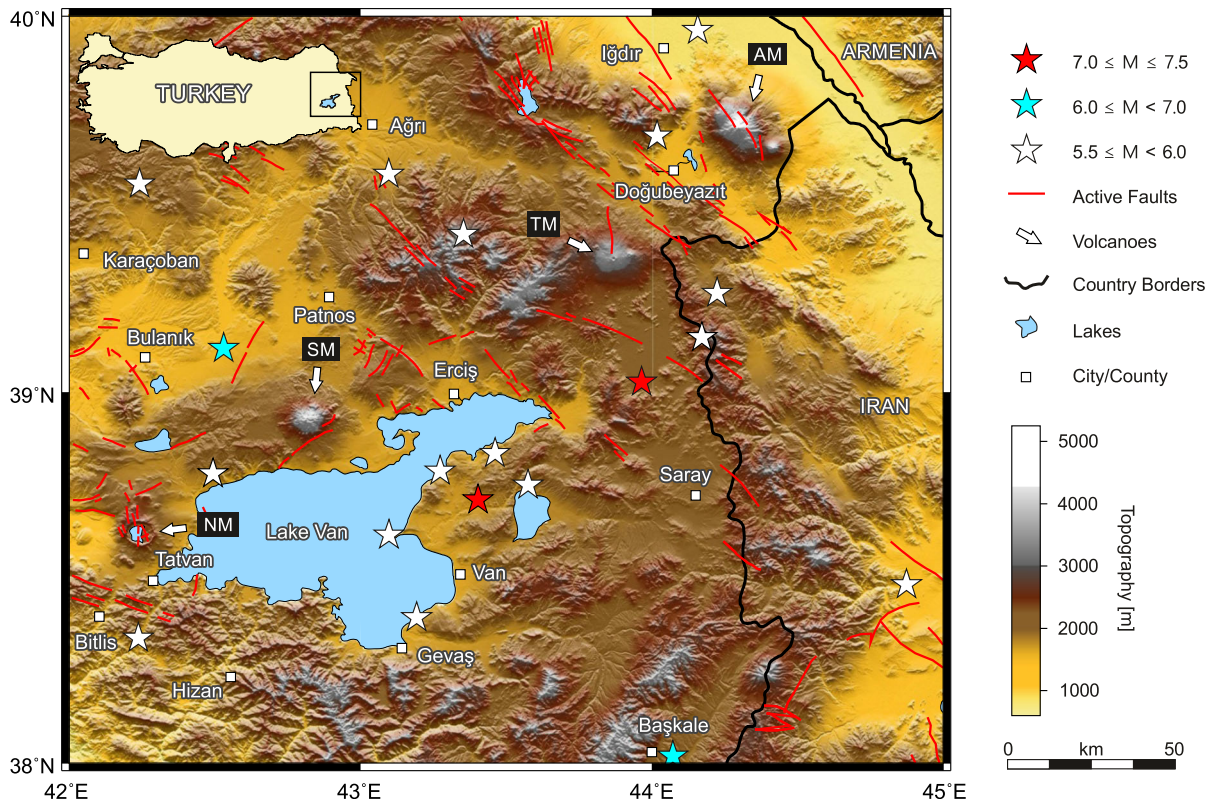
Figure 2

Location map showing the study area and surrounding. Volcanoes and the important earthquakes in the region are also shown on the map. Earthquake data were obtained from Boğaziçi University, KOERI-RETMC earthquake catalog search system (http://www.koeri.boun.edu.tr/sismo/zeqdb/). *NM* Nemrut Mountain, *SM* Süphan Mountain, *TM* Tendürek Mountain, *AM* Ağrı Mountain. The map was generated by using Generic Mapping Tools (GMT) (Wessel and Smith 1995)

zone produced rhyolite (comendite) and basalt (Ulusoy et al. 2019). This event was mentioned in the chronicles (Karakhanian et al. 2002) and the historical record (Şerefhan 1597).

Although the evolution of Mount Nemrut stratovolcano is debated, we can assure that the first volcanic activities commenced about 1.0 Ma in the early Quaternary period, with crack eruptions settling in air ducts separated by 5–10 km. The predominant activity occurred in Pleistocene and Holocene (Yılmaz et al. 1998; Ulusoy et al. 2008). Nemrut stratovolcano has a major role in the geography of Eastern Anatolia. Possibly 250 ka years ago (middle Pleistocene), an explosion occurred and actual water flow from Van Basin toward the Muş Basin was prevented because of a 60 km in length lava flow, and Lake Van known as Turkey's largest lake was formed

(Güner 1984; Karaoğlu et al. 2004). The last activity of Mount Nemrut stratovolcano has been recorded in the historical resources (Şerefhan 1597; Karakhanian et al. 2002). The historical inscription of Şerefhan (1597) describes that the activity of 1441 A.D. continued at least up to 1590's. However, the event of 1692 activity is uncertain despite being a chronicle on it (Karakhanian et al. 2002; Ulusoy et al. 2008). Eruption dates of the stratovolcano and the related events-products are schematized in Fig. 4. The historical volcanic activity during the fifteenth and sixteenth centuries (1441, 1597, and 1692 A.D in Fig. 4) can be inferred that their locations can overlap underlying shallower magma chamber(s) triggering the historical activity rather than possible and deeper other magmatic ones or evacuated magma chamber stated in Ulusoy et al. (2012) during the syn-caldera
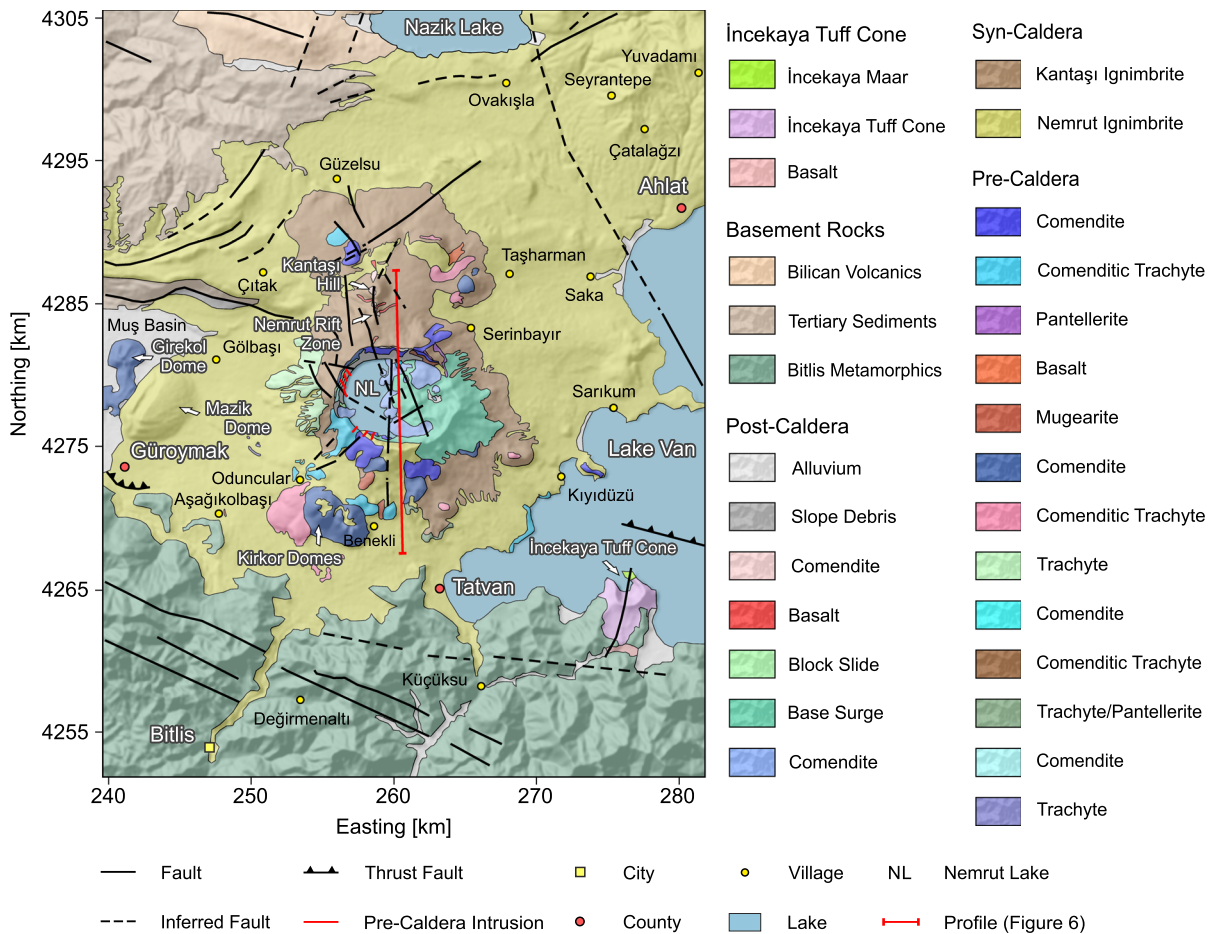
Figure 3

The geological map of the study area (simplified from Ulusoy 2008). The red line throughout the caldera is the profile used in Fig. 6. The same rocks marked with different colors indicate different ages through the evolution of Nemrut stratovolcano. The map uses Universal Transverse Mercator projection with WGS 84 datum in 38 Northern Hemisphere Zone

stage. The supported findings come from gas geochemistry (Nagao et al. 1989; Kipfer et al. 1994; Ercan et al. 1995), volcano-seismology (Ulusoy 2008), and geochemical modeling (Çubukçu 2008). According to gas geochemistry, R/R$_A$ values (where R = gas sample ^{3}He/^{4}He and Ra = air ^{3}He/^{4}He) is about 7 for Nemrut stratovolcano. Güleç et al. (2002) reported that the mantle contribution reaches a maximum at Nemrut stratovolcano in Eastern Anatolia. Volcano-seismic records around the volcano reveal an active magma chamber emplaced around the depth of 4–5 km (Ulusoy 2008). The compositional spectrum of mineral phases of all eruptive units and calculated crystallization conditions indicate that compositionally and physically zoned (~ 600 to 1050 °C) magma reservoir exists (Çubukçu 2008).

3. Data Analyses, Results and Discussion

3.1. Aeromagnetic Data Set

A national institution of Turkey named General Directorate of Mineral Research and Exploration (MTA) performed the total field aeromagnetic survey of the country between 1975 and 1989 using north–south fly paths with profile spacings of 1–2 km. In this draped-mode aeromagnetic survey the flight height, controlled by radar altimetry, was about
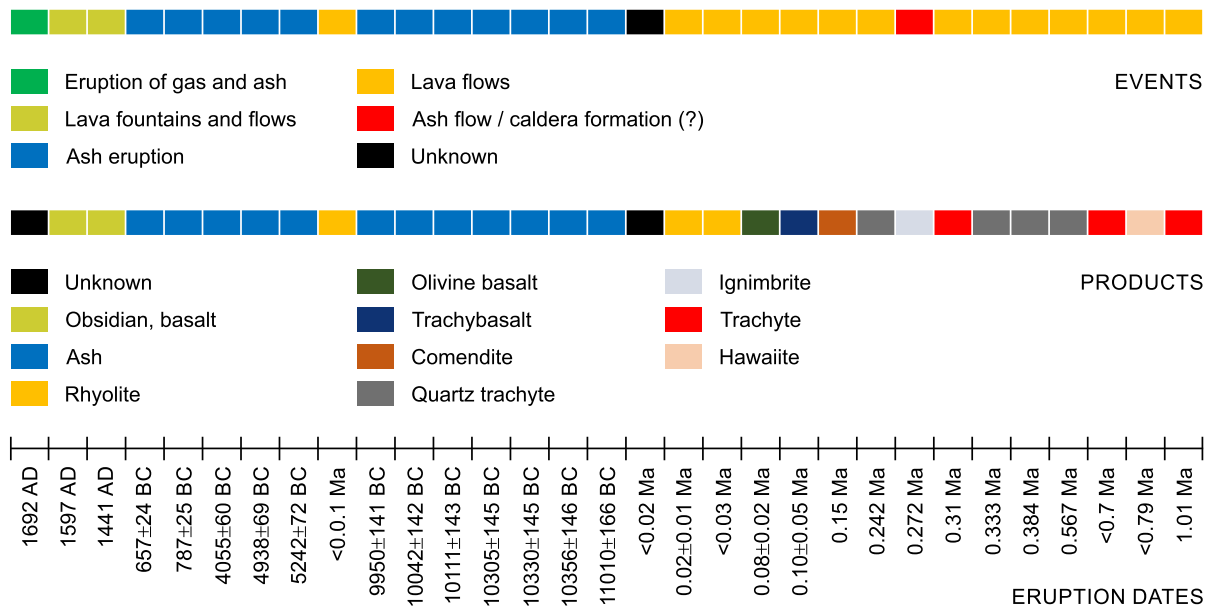
Figure 4
Eruption dates, products and events of the historical and older eruptions of the Nemrut stratovolcano (from Ulusoy et al. 2008 and the references therein)

610 m (2000 feet) from the ground surface and the data sampling along every profile was 70 m. The same institution carried out the corrections for diurnal variations and heading errors. The total field magnetic anomaly map of the entire Turkey exists in some publications (Ateş et al. 1999; MTA 2010). Here, International Geomagnetic Reference Field (IGRF, 1982.5 epoch) corrections were employed to the 1×1 km gridded data set (Fig. 5a). We used an algorithm made available by the International Union of Geodesy and Geophysics Association of Geomagnetism and Aeronomy (Baldwin and Langel 1993).

3.2. Near-Surface Magnetic Sources

It is well known that the shape of the gravity anomaly is related to the mass distribution and therefore high amplitude gravity anomalies are found on dense masses. However, the same idea is not valid for magnetic anomalies due to the added complexity caused by the directions of the magnetization and ambient field. These complexities merge a phase and distort the anomaly shapes (Blakely 1995), and necessitate the RTP technique (Baranov and Naudy

1964). The following expression transforms the magnetic anomaly (Blakely 1995).

$$\Delta T_{RTP} = F^{-1}[\psi_{RTP} \ F(\Delta T)] \tag{1}$$

where, ΔT_{RTP} denotes the RTP anomaly, F and F^{-1} represent the Fourier and inverse Fourier transforms, ψ_{RTP} denotes the RTP filter in wavenumber domain and ΔT represents the observed magnetic anomaly.

In the RTP application, we increased the data length in the grid to the next higher power of 2 by using pseudo numbers before the transformation for the elimination of possible edge effects caused by the nature of discrete Fourier transform. The added bands were neglected after the operation. Figure 5b shows the RTP image map. As previously stated, the aeromagnetic data were acquired using a draped survey mode at a constant terrain clearance, rather than at a constant elevation (level survey). Thus, almost every single data was acquired at different altitudes because of the rugged topography in the region. Drape-flying mode in aeromagnetic surveys can sometimes increase the anomaly amplitudes undesirably (Grauch and Campbell 1984), but over the strongly magnetized topographies, as in our case, this effect is generally small (Walls and Hall
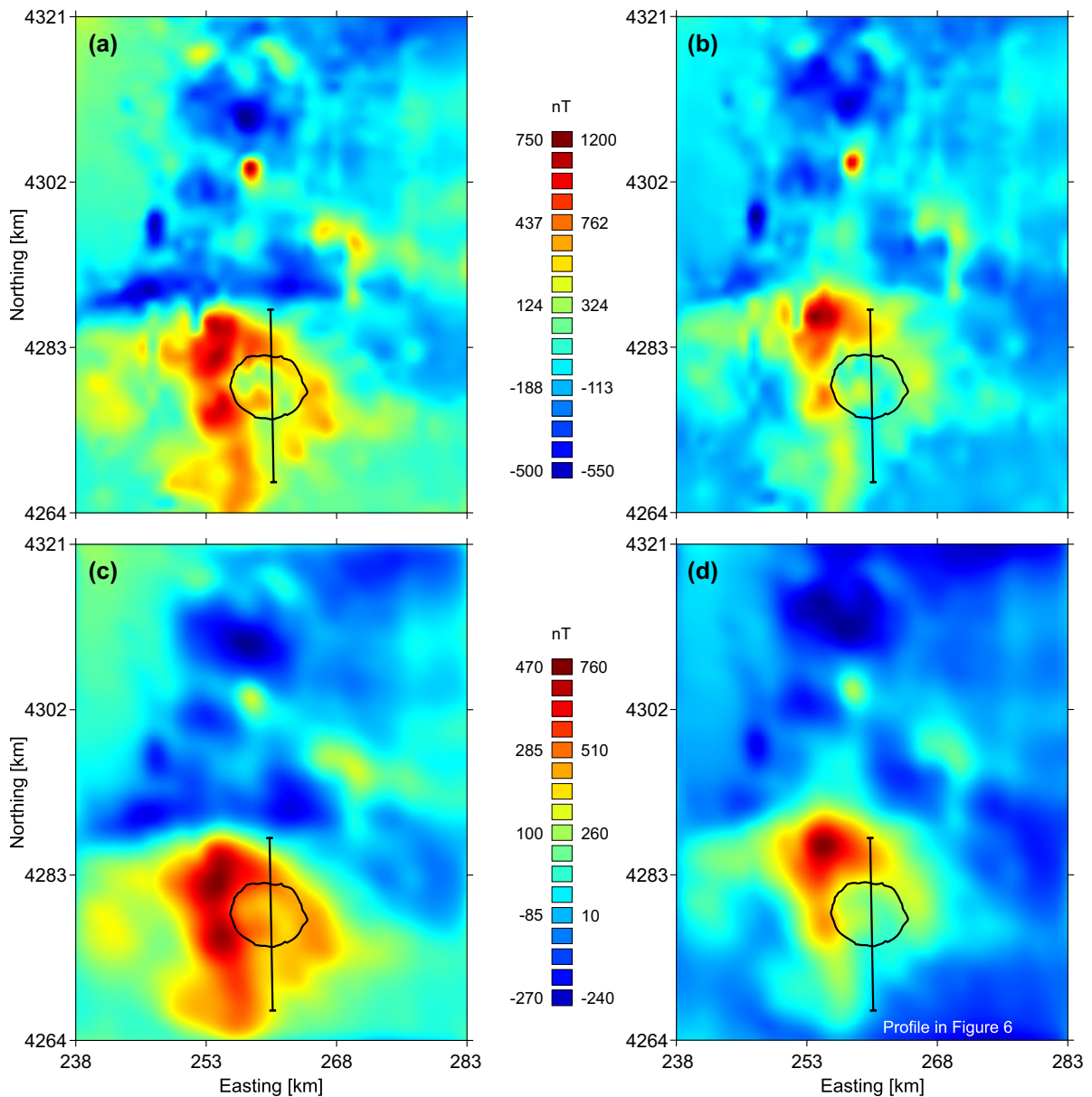
Figure 5
a Total field aeromagnetic anomaly of the study area; **b** RTP anomaly field of the data in a; **c** total field magnetic anomaly reduced to a datum horizontal plane coinciding over the highest topography; **d** RTP anomaly field of the data in **c**. The black circles on both maps indicate the rim of the Nemrut caldera. The black line throughout the caldera is the profile used in Fig. 6. The maps use Universal Transverse Mercator projection with WGS 84 datum in 38 Northern Hemisphere Zone

1998). Nevertheless, to see the effects of the draped-mode data acquisition on the magnetic anomaly amplitudes, we continued every single magnetic data upward to a datum horizontal plane coinciding over the highest topography (Fig. 5c). This approach was reported to be useful by some researchers (Grauch and Campbell 1984; Tivey et al. 1993; Szitkar and Dyment 2015; Szitkar et al. 2015). We used the following expression (Blakely 1995) to reduce every single magnetic data to a horizontal plane.
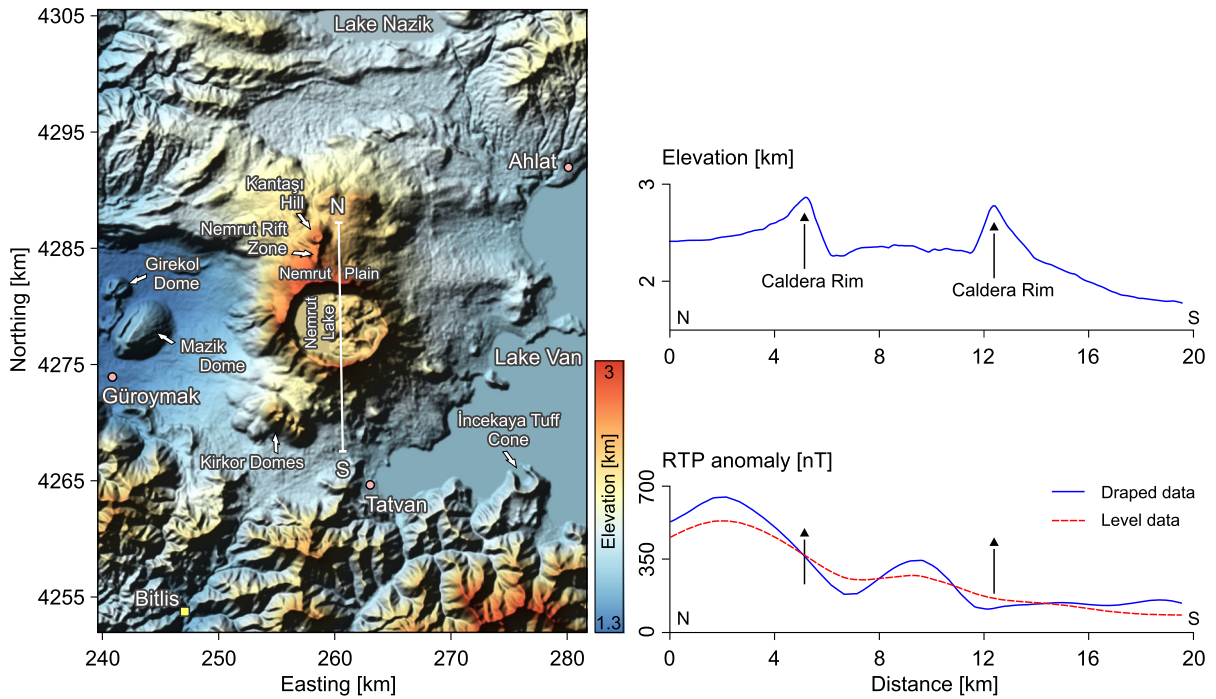
Figure 6
Left panel shows the digital elevation model of the Nemrut stratovolcano and surrounding. Right panel shows the elevation data and the RTP anomalies of the profile shown in Figs. 3 and 5. The map uses Universal Transverse Mercator projection with WGS 84 datum in 38 Northern Hemisphere Zone

$$\Delta T_{UP} = F^{-1}\left[e^{-\Delta z\,|k|}\,F(\Delta T)\right] \qquad (2)$$

where, ΔT_{UP} denotes the upward continued anomaly, e denotes the exponential function, Δz is the continuation level and k represents the radial wavenumber at grid points. Possible edge effects were removed as explained previously. The new RTP anomaly map (Fig. 5d) was obtained using the data reduced to a horizontal plane. The comparison of two RTP maps shows that although the magnetic anomalies in the new RTP map are in smoother form resulting in a loss of some high frequencies, the main magnetic highs in the vicinity of the caldera rim do not change significantly. To understand the effects of two different data types in detail, we compared topographic data and two RTP data sets of Nemrut stratovolcano through a north–south directed profile (Fig. 6). It is seen that sharp topographic changes do not produce too severe spurious phases in the anomaly amplitudes in our case. High amplitude magnetic anomalies of the draped and level data seen in the beginning of the profile and between the caldera rims are in consistent

with each other. These two aeromagnetic data acquisition techniques have both superior and weak sides to each other, which were well explained in Grauch and Campbell (1984). To avoid misleading interpretation, the data acquired via drape-mode flying should be reduced into the level data or vice versa for a comparison before the grid operation steps (Grauch and Campbell 1984).

The north–south trending magnetic highs located at west of caldera rim (black ellipse) in Fig. 5a, c are shifted northwest and west of the caldera in the RTP maps (Fig. 5b, d). High and moderate magnetic anomaly patterns still exist at north and east of the caldera, respectively. Relatively lower magnitude magnetic values dominate south of the caldera. There is no overlap between the caldera position and the high amplitude magnetic anomalies. This case indicates that the magnetized sources causing the high amplitude anomalies are not beneath the caldera's location exactly. The magnetic highs located north and northwest of the caldera rim are most likely due

to Kantaşı ignimbrite (Fig. 3). Kantaşı ignimbrite located north of the caldera rim produces high-amplitude magnetic values over the profile while Nemrut ignimbrite shows relatively low magnetic anomalies (Fig. 6). Kantaşı and Nemrut ignimbrite series are the product of the caldera-forming (syn-caldera) eruptions. The collapse of the caldera occurred due to the catastrophic pyroclastic eruption related to evacuation of the magma chamber during the syn-caldera aged between ca. 90–30 ka (Çubukçu et al. 2012). The pyroclastic series of Kantaşı ignimbrite (Ulusoy et al. 2008) spread in the northern part of the volcano and on the Kantaşı hill. The rift activity occurred north of the caldera rim between Nemrut plain and Kantaşı hill (Fig. 3). Kantaşı ignimbrite covers the ridge through the rift and its adjacent areas. Along the ridge with fractured and cracked Kantaşı ignimbrite, lava flowed over them. The activity marked by lava fountains and flow occurred in the northern end of the rift identifying the latest volcanic activity of 1441 A.D. continued at least up to 1597 A.D. (Şerefhan 1597; Karakhanian et al. 2002). This activity is bimodal rift activity

produced comendites and basalts (Ulusoy et al. 2012). Therefore, high amplitude magnetic anomalies observed north of the caldera rim (Fig. 6) are most likely associated with these exposures of comenditic and basaltic flows. The anomaly peak located at the beginning of the profile (Fig. 6), in both draped and level data, is in excellent agreement with the location of the flows along the Nemrut rift zone. On the other hand, although Nemrut ignimbrite covers the largest area in comparison to the other products of the Nemrut stratovolcano (Ulusoy et al. 2008) and it extends to the northeast and western shorelines of Lake Van, there has not been such an activity in the area, as also confirmed by magnetic anomalies having relatively low amplitudes. The moderate increase of the magnetic anomalies between the caldera rims (Fig. 6) is associated with intra-caldera lava flows, domes, and eruptions represented by comendite type lava and ash. These results show that high-frequency surface/near-surface sources in the study area have remarkable effects on the amplitudes of airborne magnetic anomalies. We performed an edge approx-imation procedure to better understand abrupt lateral
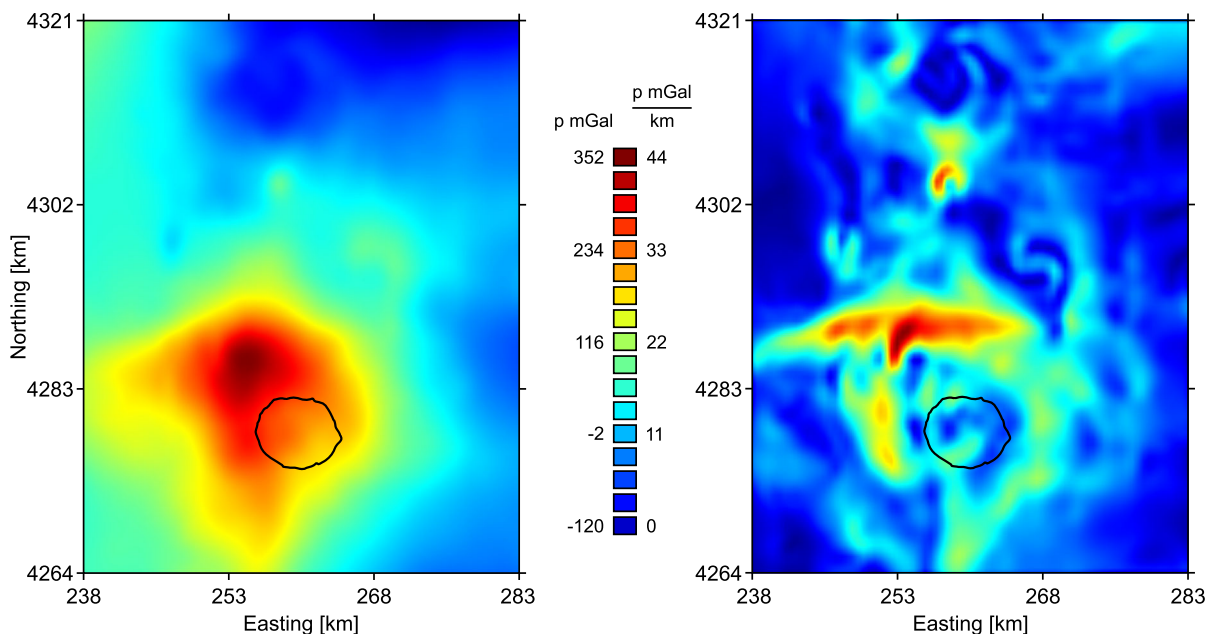

Figure 7
Left panel illustrates the PSG anomaly map of the data shown in Fig. 5a, and right panel illustrates the THD anomaly map of the data in the left panel. The black circles on both maps indicate the rim of the Nemrut caldera. The maps use Universal Transverse Mercator projection with WGS 84 datum in 38 Northern Hemisphere Zone

changes in magnetization by transforming the magnetic data to PSG anomalies and then calculating the THD amplitudes (Cordell and Grauch 1985; Blakely 1995). The following formulation produces the PSG anomaly (Blakely 1995).

$$\Delta T_{PSG} = F^{-1}[\psi_{PSG} F(\Delta T)]\omega \qquad (3)$$

where, ΔT_{PSG} is the PSG anomaly, ψ_{PSG} denotes the linear PSG filter in wavenumber domain and ω represents the constant term expressed in Blakely (1995). We eliminated possible edge effects as explained previously. PSG image map (Fig. 7 left panel) exhibits a smoother anomaly pattern of the study area. Since the computation of the horizontal derivatives in space domain is more favorable than doing in wavenumber domain (Arısoy 2014; Ekinci 2017), we used the following simple finite difference approach to obtain THD anomalies.

$$THD = \left[\left(\frac{\partial \Delta T_{PSG}}{\partial x} \right)^2 + \left(\left(\frac{\partial \Delta T_{PSG}}{\partial y} \right)^2 \right) \right]^{1/2} \qquad (4)$$

where,

$$\frac{\partial \Delta T_{PSG}(x,y)}{\partial x} \approx \frac{\Delta T_{PSG}(i+1,j) - \Delta T_{PSG}(i-1,j)}{2\Delta x} \qquad (5)$$

$$\frac{\partial \Delta T_{PSG}(x,y)}{\partial y} \approx \frac{\Delta T_{PSG}(i,j+1) - \Delta T_{PSG}(i,j-1)}{2\Delta y} \qquad (6)$$

where, i and j are the discrete values of the PSG anomaly on the grid surface at uniform data spacings Δx and Δy. THD image map (Fig. 7 right panel) shows that the highest amplitudes are located north of the caldera rim. A detailed look at the THD map and the surface geology map of the region (Fig. 3) indicates that the rapid lateral changes in the magnetization located north of the caldera rim are due to contact between Nemrut and Kantaşı ignimbrites. In addition, some high THD amplitudes also exist in the contacts of these units in other parts of the study area. On the other hand, although Kantaşı ignimbrite does not reach to the western tip of the Lake Van (Fig. 3), we observe moderate amplitude THD anomalies in this area. Magnetic anomalies are evident west of the caldera rim as well (Fig. 5b, d).

THD image map (Fig. 7 right panel) also indicates some abrupt lateral changes in magnetization. These high anomalies are most likely due to trachyte which is a product of the pre-caldera stage of the Nemrut volcanism (Fig. 3). Additionally, magnetic highs cover a larger area than trachyte as seen in the geology map (Fig. 3). Thus, it is reasonable to mention that pre-caldera trachyte extends westward beneath the Nemrut ignimbrite. Ulusoy et al. (2008) reported some relatively high thermal anomalies west of the caldera rim. These thermal anomalies show positive surface kinetic temperature values. Compatibility is evident between surface temperatures and magnetic anomalies at that part of the study area. Therefore, another possible interpretation of the magnetic anomalies seen west of the caldera rim is the presence of hydrothermal activities. A thermal spring around Güroymak county located about 12 km west of the caldera rim supports this idea. It is well-known that hydrothermal effects tend to increase or decrease magnetic properties based on some parameters such as fluid and host rock composition, oxidation ratio, temperature of alteration, etc. (e.g. Grant 1985; Pilkington and Hildebrand 2000; Tivey and Dyment 2010). Hence, high amplitudes seen west of the Nemrut caldera rim (Figs. 5b, d and 7 right panel) are likely due to the structural elements (faults) lying from the inner caldera or the top of the caldera rim towards western flanks of the volcano (Fig. 3). That is, the structural elements may be the
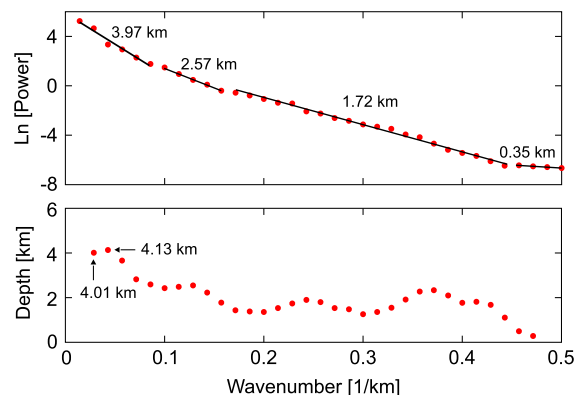

Figure 8
Upper panel shows the radially averaged power spectrum analysis of the magnetic data, and lower panel shows the depth estimation calculated by averaging the slope of the energy spectrum over five points. Depth values include flight height

main pathways controlling the circulation of hydrothermal fluids with to the shallow groundwater into the ignimbrite and pre-caldera trachyte. In the region, total dissolved solid (TDS) is higher for hydrothermal fluid than peripheral cold-water body (Kurttaş and Tezcan 2018). Although Fe concentration was not reported, we assume that TDS most likely contains total Fe concentration in hydrothermal fluid due to metaluminous rocks covering the region.

3.3. Deep-Seated Magnetic Sources

We performed power spectrum analysis to estimate the depths of deeper magnetized sources. The slopes in the power spectrum plots are associated with the depths of magnetized bodies (Spector and Grant 1970). In the notation of Blakely (1995), energy spectrum of block ensembles, consisting of shallow and deeper sources, is defined as following.

$$|F(k)|^2 = 4\pi^2 C_m^2 |\theta_m|^2 |\theta_f|^2 M_0^2 \, e^{-2|k|zt}$$
$$\left(1 - e^{-|k|(Zb-Zt)}\right)^2 S^2(a,b) \qquad (7)$$

where, C_m is a constant, θ_m and θ_f denote the factors related to the direction of magnetization and magnetic field, respectively, M_0 denotes magnetization, Zt and Zb are the top and the bottom depths of the magnetized bodies, respectively, and $S^2(a,b)$ is associated with the horizontal dimensions of sources. The top depths of the sources are estimated by fitting segments to the power spectrum plots. Figure 8 shows radially averaged power spectrum results in

the wavenumber domain obtained through Oasis Montaj software (Geosoft Inc.). The depth of the deeper magnetized sources is 3.97 km (including the flight height) derived by the first slope shown in the upper panel. The depth estimations demonstrated in the lower panel show the average values of the slopes of the energy spectrum over five points. We obtained a depth of about 4.13 km (including the flight height) for the deeper sources based on averaging. Thus, we assume that the shallowest deep-seated magnetic sources are located about 4 km below the flight hight. Additionally, we also considered the possible ambiguities of the power spectra technique described by Quarta et al. (2000). Therefore, to avoid a contradiction we followed another technique proposed by Zeng et al. (2007). In this technique to minimize the effects of the short-wavelength sources, the optimum upward continuation level is determined by a statistical approach. Firstly, a series of continuation heights is determined and then the correlation coefficients between the upward continued data at two successive heights are calculated. Continuation height providing the maximum deflection of these coefficients is assumed to be optimum continuation level (Zeng et al. 2007). We calculated the correlation coefficient between the upward continued data at two successive heights by the following definition.

$$R_{A,B} = \frac{\sum_{i=1}^{m} \sum_{j=1}^{n} (A_{mn} - \bar{A})(B_{mn} - \bar{B})}{\left[\left(\sum_{i=1}^{m} \sum_{j=1}^{n} (A_{mn} - \bar{A})^2\right)\left(\sum_{i=1}^{m} \sum_{j=1}^{n} (B_{mn} - \bar{B})^2\right)\right]^{1/2}}$$
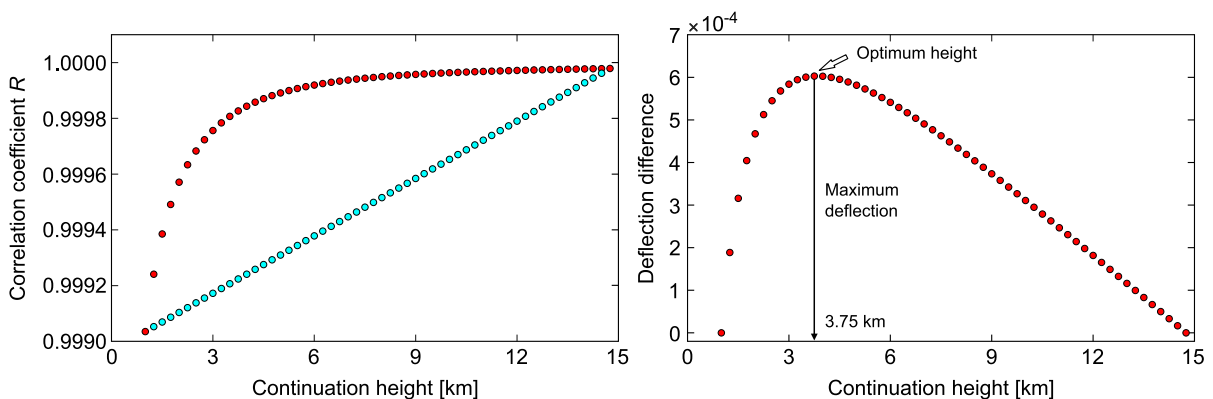$$(8)$$

Figure 9
Left panel illustrates the correlation coefficients between the upward continued data sets at successive heights, and right panel illustrates the maximum deflection showing the optimum continuation height
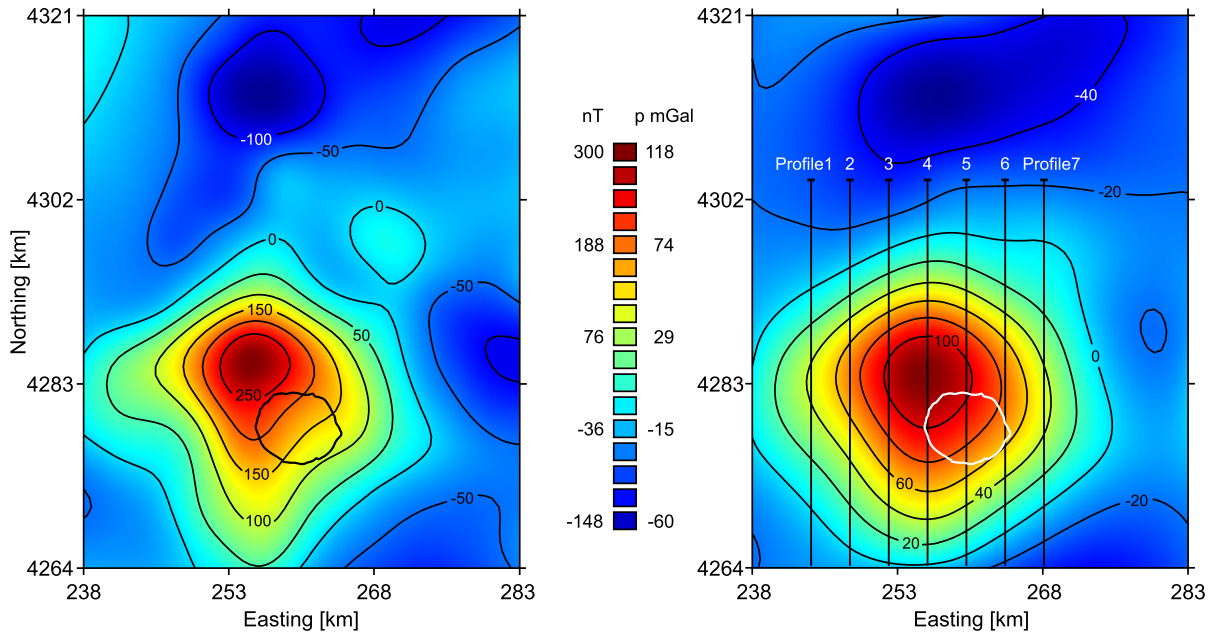
Figure 10
Left panel shows the upward continued anomaly map of the data shown in Fig. 5b, and right panel shows the PSG anomaly map of the data in the left panel. The black lines on the map indicate the NFG profiles. The black circles on the maps indicate the rim of the Nemrut caldera. The maps use Universal Transverse Mercator projection with WGS 84 datum in 38 Northern Hemisphere Zone

where, A and B are the upward continued data obtained at two successive heights, $\bar{A}$ and $\bar{B}$ represent their average values, respectively. We used a vector of linearly spaced heights between 1 and 15 km with an increment of 0.25 km. Figure 9 left and right panels demonstrate the correlation coefficients and the maximum deflection height of our case, respectively. The approach yielded an optimum continuation height of 3.75 km. Considering the results of power spectrum analyses and statistical approach, we preferred 4 km height for upward continuation process to minimize high-frequency near-surface effects and to analyze the deep-seated sources. Figure 10 left panel shows upward continued RTP anomaly map. Short-wavelength anomalies caused by surface/near-surface magnetized sources seen in Fig. 5b, d are remarkably attenuated, whereas anomalies of the underlying deeper sources are more accentuated. We carried out a three-dimensional inversion procedure to understand the subsurface distributions of deep-seated structures causing strong magnetic anomalies shown in Fig. 10 left panel. The inversion procedure (Cordell and Henderson 1968) supposes that the sources causing gravity anomalies

can be approximated by an assemblage of infinitely extending vertically-sided prisms having a uniform density. The following definition produces the approximate gravity anomaly of any vertically-sided prism element below any observation point on the grid plane.

$$\Delta g = \gamma \rho s^2 \left[\frac{1}{(R^2 + d^2)^{1/2}} - \frac{1}{\left(R^2 + (d+t)^2\right)^{1/2}} \right] \tag{9}$$

where, γ denotes the gravitational constant, ρ represents the density of the prism element, s is the grid spacing, R represents the distance between corresponding grid node and the prism element beneath the grid plane, and d is the depth to the top of the prism element having a thickness of t. Here, an improved form of the procedure (Kearey 1991) which has been successfully performed to airborne magnetic anomalies due to igneous rocks (e.g. Kearey 1991; Ates and Kearey 1993, 1995; Ates et al. 1997; Büyüksaraç et al. 2005; Bektaş et al. 2013; Balkaya et al. 2017) was used. Firstly, we transformed the
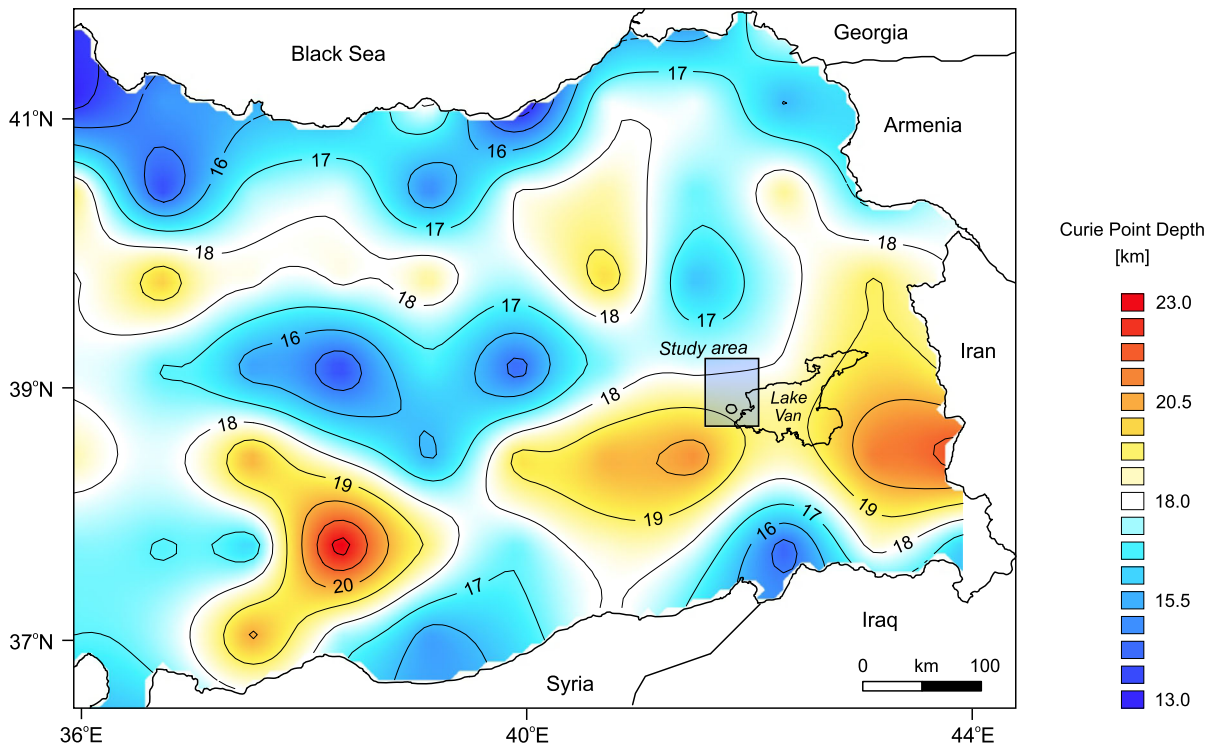
Figure 11

CPD map of the eastern Turkey. The black rectangle shows the study area and the circle inside it indicates the rim of the Nemrut caldera
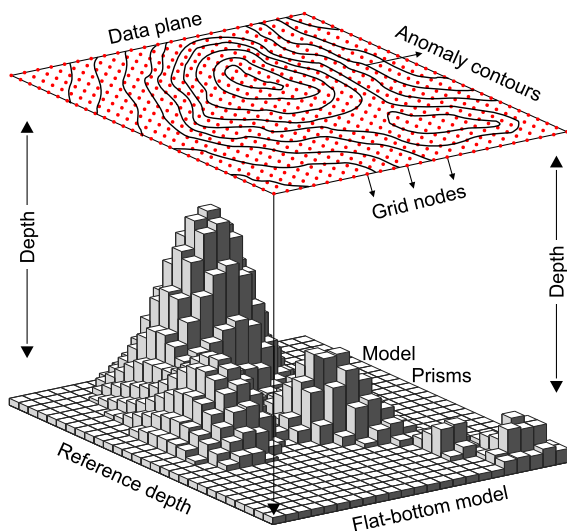

Figure 12

The schematic representation of the inversion procedure showing a synthetic flat-bottom model

the PSG image map (Fig. 10 right panel). We inverted the PSG data set using 2668 vertical prisms (58 rows × 46 columns). In this inversion approach, a horizontal reference plane is determined to delimit either top, midpoint or bottom depths of the prism elements. Since this step necessitates a priori information for a more realistic interpretation, Curie-point depths (CPD) of the eastern Turkey (Bektaş et al. 2007) were taken into consideration. The average CPD of the study area is 19 km (Fig. 11). Thus, we used a flat-bottom model having a depth of 19 km assuming that the bottom depths of the vertically-sided prisms accord with the depth of the Curie isotherm. Figure 12 illustrates the schematic representation of this procedure. The inversion process was performed using a uniform ratio of the intensity of magnetization to density (Kearey 1991). To determine the depths of the prisms located over the grid points in the reference plane, we produced an initial model involving 2668 vertical prisms through the Bouguer slab formula (Bott 1960) given below.

upward continued data into PSG data. After removing the added pseudo-random data bands, we produced
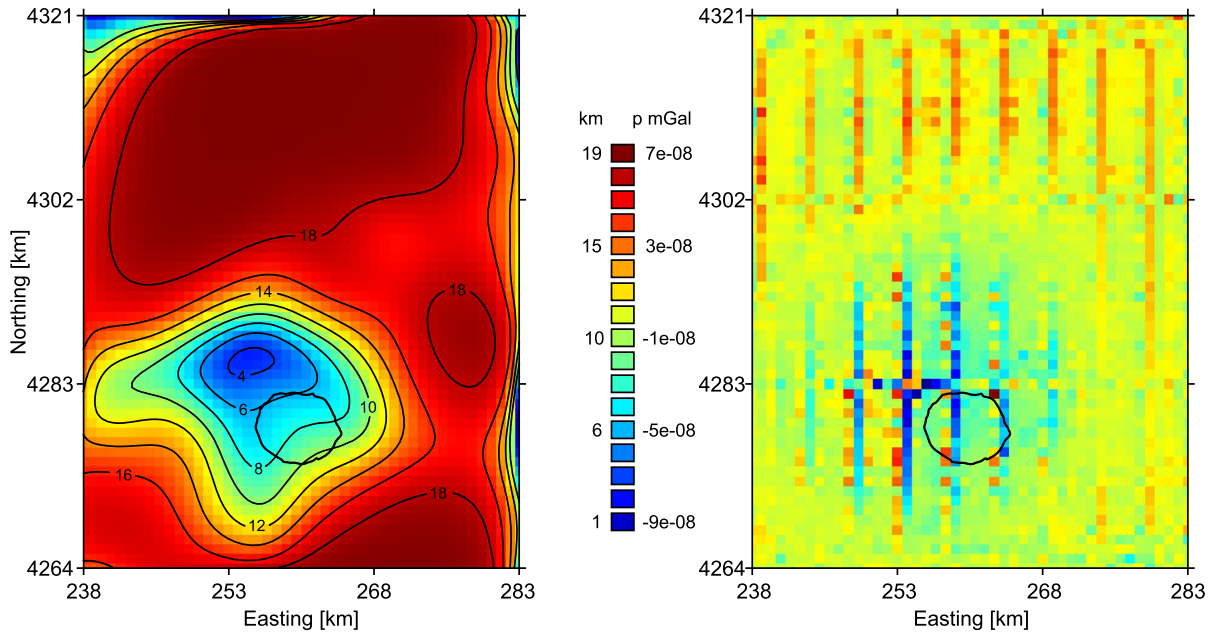
Figure 13
Left panel shows the three-dimensional magnetic model of the study area, and right panel shows the difference between observed and calculated PSG anomalies. The black circles on the maps indicate the rim of the Nemrut caldera. Depth values include flight height. The maps use Universal Transverse Mercator projection with WGS 84 datum in 38 Northern Hemisphere Zone

$$T(x,y) = g_{obs}(x,y)\frac{1}{2\pi\gamma\rho} \qquad (10)$$

where, x, y are the coordinates of the reference plane, g_{obs} represents the observed anomaly, and the other terms were given previously. The RMS value between the observed and calculated data was the lowest at the end of the 8th iteration. Figure 13 left panel shows the inverse magnetic model produced using the top depths of the prisms. The image map of the difference between observed and calculated data indicates a satisfactory solution (Fig. 13 right panel). The thickest prisms lying on the reference plane have a depth of about 3.6 km including the flight height, which is close to the power spectrum result (about 4 km). At the final step, we performed two-dimensional NFG technique through seven parallel profiles extracted from the PSG anomaly map (see Fig. 10 right panel for the locations of the profiles). The NFG technique combines downward continuation and analytic signal. The technique yields satisfactory results in the estimation of the causative body location and depth using geophysical anomalies (Pašteka 2000; Zeng et al. 2002; Aydin 2007; Oruç and

Keskinsezer 2008; Sındırgı et al. 2008; Aghajani et al. 2010; Ekinci and Yiğitbaş 2012, 2015; Sheng and Xiaohong 2015; Ekinci et al. 2017; Soleimani et al. 2018; Elysseieva and Pašteka 2019; Pamukçu et al. 2019; Sındırgı and Özyalın 2019). The following definition produces the dimensionless amplitude of the two-dimensional NFG at any point over x-profile (Berezkin 1967, 1973).

$$NFG(x_i,z_j) = \frac{\left[\left[\left(\frac{\partial V(x_i,z_j)}{\partial x}\right)^2 + \left(\frac{\partial V(x_i,z_j)}{\partial z}\right)^2\right]^v\right]^{1/2}}{\frac{1}{M}\sum_{i=1}^{M}\left[\left[\left(\frac{\partial V(x_i,z_j)}{\partial x}\right)^2 + \left(\frac{\partial V(x_i,z_j)}{\partial z}\right)^2\right]^v\right]^{1/2}}$$
$$(11)$$

where, $NFG(x,z)$ is the dimensionless amplitude, x_i is the data location over the measuring profile, M denotes the data length, z_j is the continuation depth, and v is an operator controlling the values and the width of the maximum anomaly (Sındırgı et al. 2008). We obtained the directional derivatives using the following definitions (Berezkin 1988).
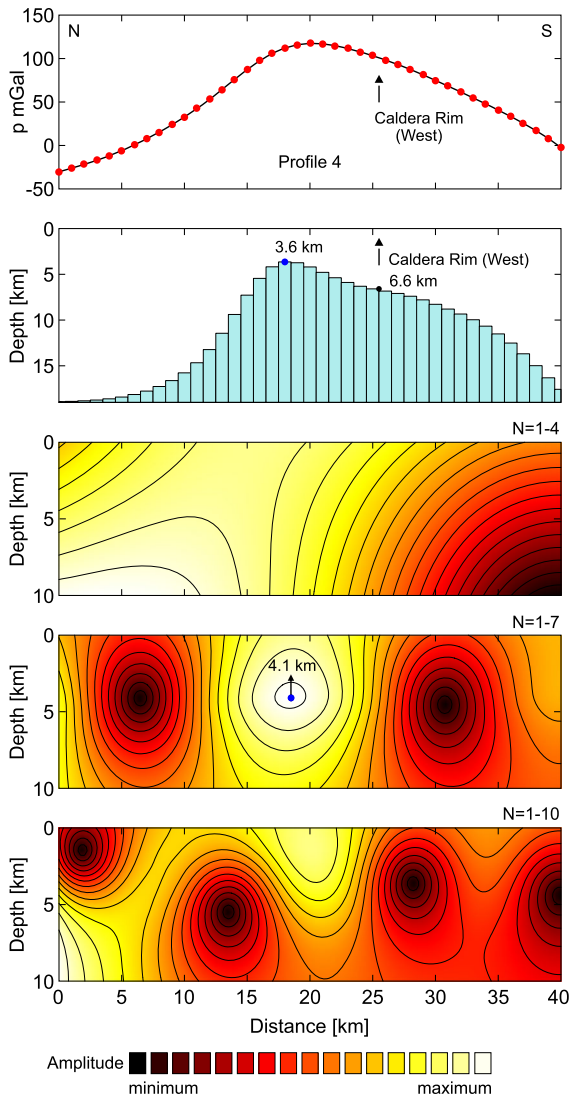
Figure 14
PSG anomaly, causative blocks obtained from three-dimensional inversion and NFG solutions of profile 4 shown in Fig. 10 right panel. Depth values include flight height

$$\frac{\partial V(x,z)}{\partial x} = \frac{\pi}{L} \sum_{n=1}^{N} nB_n \cos\left(\frac{\pi nx}{L}\right) e^{\pi nz/L} q \qquad (12)$$

$$\frac{\partial V(x,z)}{\partial z} = \frac{\pi}{L} \sum_{n=1}^{N} nB_n \sin\left(\frac{\pi nx}{L}\right) e^{\pi nz/L} q \qquad (13)$$

where,

$$B_n = \frac{1}{L} \int\limits_{-L}^{L} V(x,0) \sin\left(\frac{\pi nx}{L}\right) dx \qquad (14)$$

$$q = \left[\sin\left(\frac{\pi n}{N}\right) \Big/ \frac{\pi n}{N} \right]^{\mu} \qquad (15)$$

where, B_n denotes the Fourier sine coefficient, q represents the Lanczos smoothing term and it removes Gibbs effect, n is the harmonic number, and the parameter μ controls the curvature of the q (see Berezkin (1967) for more details). In NFG amplitude maps contour lines are examined to find the optimum harmonic limits. The main local maximum represented by fully closed symmetric contours generally indicates the spatial parameters of the causative body (e.g. Berezkin 1967; Aydin 2007; Sındırgı et al. 2008; Ekinci et al. 2017). Here, we determined the optimal harmonic limits by some trial-and-error applications. Firstly, trying different harmonic limits we applied the NFG procedure to profile 4 which represents the highest amplitude anomaly. Figure 14 shows the results of the NFG technique and fully closed contour lines are evident in the harmonic limit of $N = 1 - 7$. The local maximum indicates a depth of 4.1 km (including the flight height) for the causative source. This finding supports the results of power spectrum analysis, statistical approach and three-dimensional modelling scheme. We analyzed the other profiles using the same optimum harmonic limits. Figures 15, 16 and 17 show that the source depths determined through the NFG and inversion techniques are compatible with each other. Thus, it is reasonable to mention that the causative blocks are located about between 3.0 and 3.5 km below the ground surface. These depth values gradually increase towards Kantaşı hill and Nemrut caldera. Ulusoy (2008) suggested the presence of a shallow magma chamber at the depth of 4–5 km in the vicinity of Nemrut caldera based on seismological data. He reported that shallow and magma chamber related volcanogenic earthquakes are mostly occurred at these depths. Also, there is no observed seismological event above these depths in the close vicinity of the Nemrut caldera (Fig. 18). Hence, we mention that the emplacement of the shallow magma chamber is most likely above these magnetized blocks located between Kantaşı hill and Nemrut caldera.
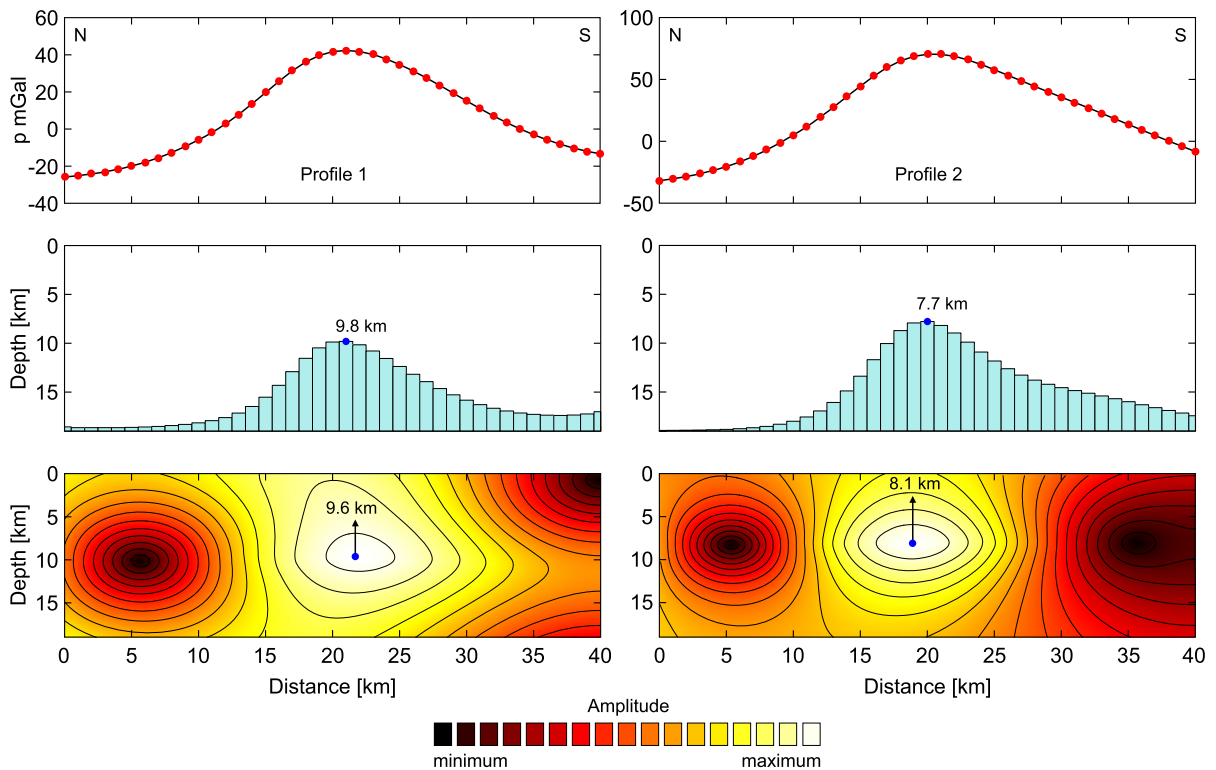
Figure 15
PSG anomaly, causative blocks obtained from three-dimensional inversion and NFG solutions of profiles 1 and 2 shown in Fig. 10 right panel. Depth values include flight height

4. Conclusions

In this study, we investigated Mount Nemrut stratovolcano (Bitlis, Eastern Turkey), a quiescent volcano located close to the continental–continental collision boundary (Bitlis–Zagros suture zone), through total field aeromagnetic anomalies. We performed some linear transformations, total horizontal derivative technique, power spectrum analysis, a statistical approach, three-dimensional inversion procedure and two-dimensional NFG technique to better understand the nature of the magnetized sources beneath the stratovolcano and the surroundings. We determined that short-wavelength anomalies having moderate-high amplitudes in the area close to the Nemrut caldera are in good agreement with the

geology map of the studied area. Strong magnetic highs located north of the caldera rim are linked to short- and long-wavelength anomaly sources. In this area, the exposures of comendite and basaltic flows related to bimodal rift activity on the Kantaşı hill contribute to the increasing of magnetic anomaly field. Another anomaly pattern located west of the caldera rim is most likely associated with the pre-caldera trachyte which extends over a larger area than it appears on the surface geology map. Additionally, the presence of hydrothermal fluids may have an effect on the increase of amplitudes. It should be noted that TDS amount is higher in hydrothermal fluid which probably contains total dissolved Fe due to metaluminous rocks covering the investigated region. Structural elements of faults contribute an
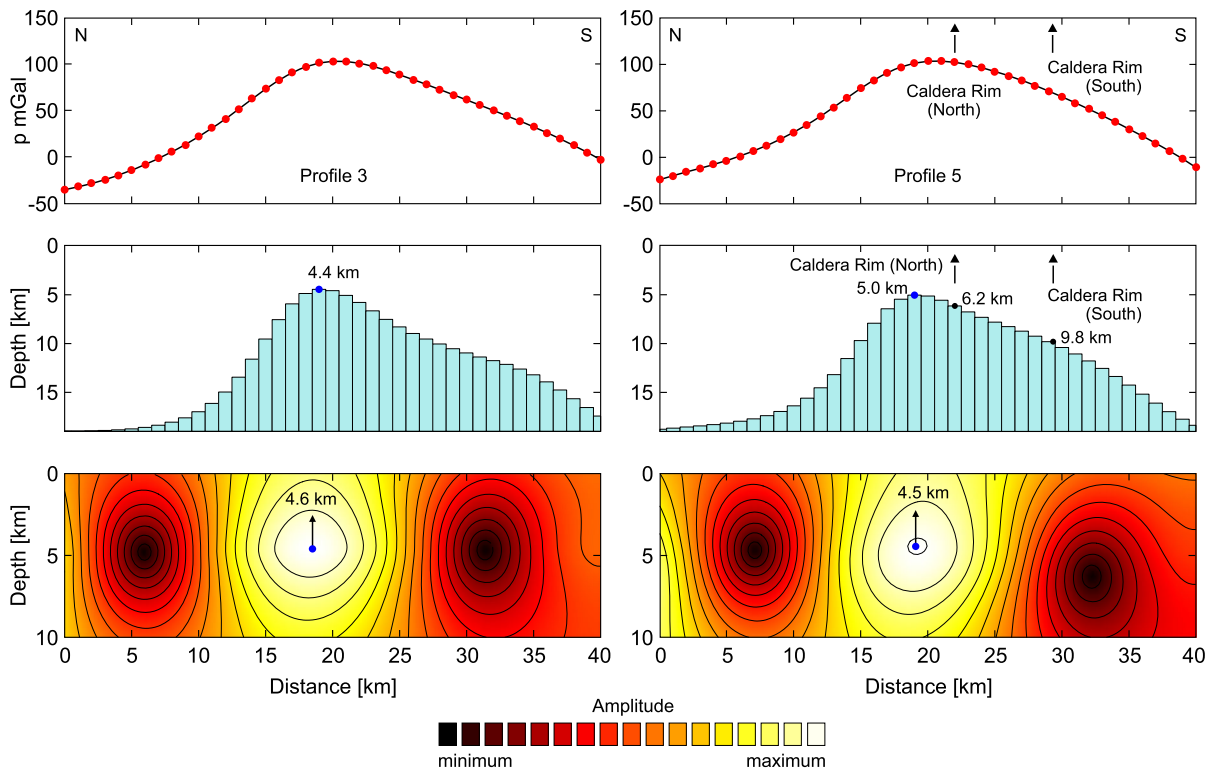
Figure 16
PSG anomaly, causative blocks obtained from three-dimensional inversion and NFG solutions of profiles 3 and 5 shown in Fig. 10 right panel. Depth values include flight height

upward movement of hydrothermal fluids to shallow depths there and bring about mixing of cold-less mineralized water body with higher mineralized hydrothermal fluids into porous of Nemrut and Kantaşı ignimbrites and pre-caldera trachyte. High thermal values determined from ASTER surface kinetic temperatures (Ulusoy et al. 2008) and the presence of a thermal spring around the area are supportive of this finding. Relatively high amplitude magnetic anomalies exist east of the caldera rim. The mineral assemblage of Nemrut eruptive products range from metaluminous including Fe–Ti oxides (basalt, mugearite) to peralkaline (rhyolite) types (Çubukçu 2008). Thus, widespread Fe-rich rocks have a significant influence on increasing the magnetic anomaly values in the investigated area. We minimized the high-frequency effects through an appropriate upward continuation level based on the information obtained from the power spectrum analysis and a statistical approach. CPD-assisted three-

dimensional inversion procedure of PSG anomalies revealed the depths of deep-seated source ensembles. These deep-seated sources are the highly magnetized wholly crystallized and solidified mass ensembles extending from just above the Curie temperature isotherm to the depths shown in Fig. 13 left panel. The depth of the top of the shallowest magnetized mass is about 3.0 km from the ground surface, which is highly compatible with the solution of power spectrum analysis (about 3.4 km). Additionally, two-dimensional NFG solutions of the seven profiles extracted from PSG anomalies provided insight into the depths of these deep-seated sources. Profile 4 passing over the highest amplitude PSG anomaly revealed about 3.5 km depth for the shallowest geologic source from the ground surface. The depths of the magnetic sources determined from NFG solutions of other profiles are also in harmony with the results of the inversion procedure. The seismological data show that magma chamber related volcanogenic
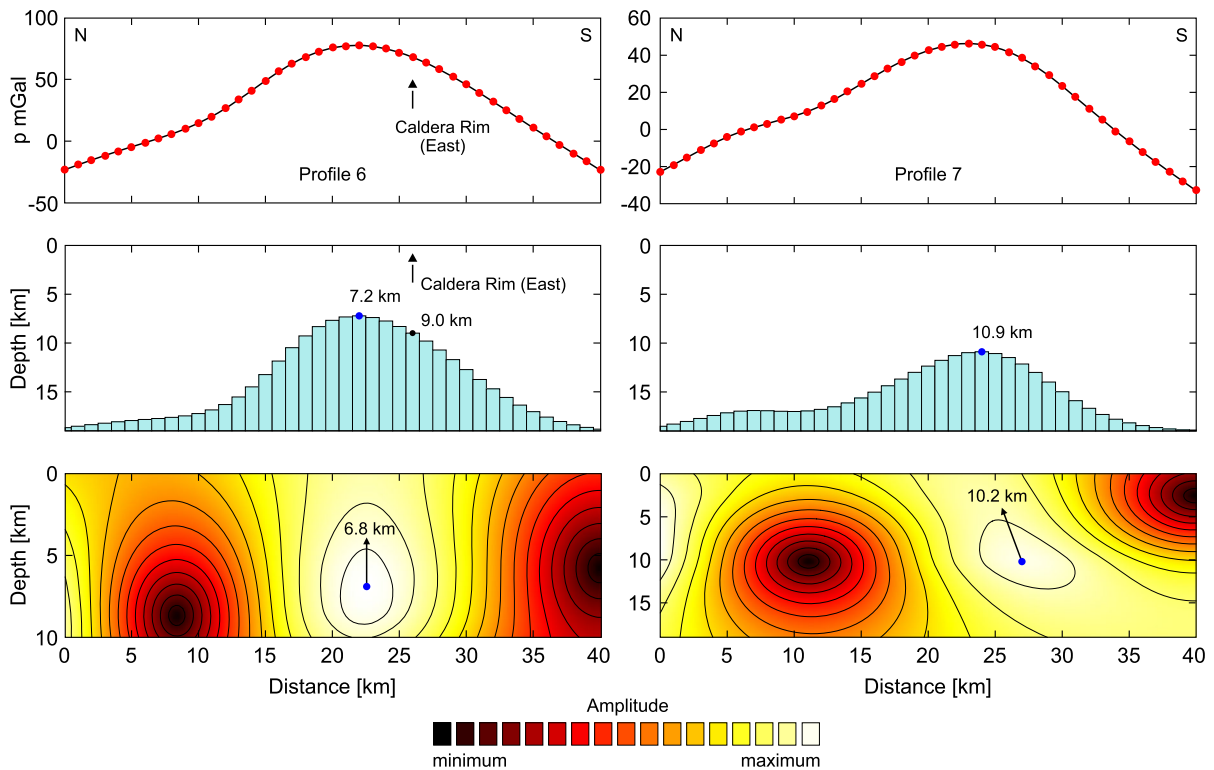
Figure 17
PSG anomaly, causative blocks obtained from three-dimensional inversion and NFG solutions of profiles 6 and 7 shown in Fig. 10 right panel. Depth values include flight height

earthquakes occurred mostly at depth of 4–5 km around the caldera (Ulusoy 2008). These volcanogenic earthquakes were not observed at shallower depths (Fig. 18). Additionally, the top depths of the crystallized and solidified deep-seated rock masses determined through inversion and NFG techniques do not contradict the presence of a magma chamber at depth of 4–5 km in the vicinity of Nemrut caldera and Kantaşı hill. Also, this location overlaps with the activity of 1441 A.D. to 1597 A.D. (Şerefhan 1597; Karakhanian et al. 2002) through Nemrut rift zone where comendite and basalt of the post-caldera stage (Fig. 3) erupted. The spectrum of mineral phases of all eruptive units and the calculated crystallization conditions indicate that a compositional and physical zoned magma reservoir can exist, having a temperature range of ∼ 600 to 1050 °C (Çubukçu 2008). This temperature zonation is higher than the Curie temperature, at which the rocks do not produce observable magnetic responses. Therefore,

we could not obtain solidified and magnetized blocks lower than 4–5 km depths near the caldera and the rift zone. Besides, the lithostatic gradient of 1.5 kbar (≈ 0.3kbar/km) reported by Çubukçu (2008) also indicates a depth of 5 km for the magma chamber. We note that the shallow magma chamber mentioned herein triggered the post-caldera stage products of rhyolite (comendite) and basalt which outcrop around Kantaşı hill (Fig. 3) and we emphasize that the shallow magma chamber does not mean the evacuated magma chamber (Çubukçu et al. 2012) during the syn-caldera stage.

Nemrut stratovolcano, as regards the regional geology context of Eastern Anatolia, situated on the eastern end of the Muş basin. The basin (Fig. 3) is the deformed and remnant segment of the WNW trending Oligo-Miocene Muş-Van basin (Koçyiğit et al. 2001) which is located at the northern foot of the Bitlis–Zagros suture zone (Bitlis metamorphics in Fig. 3). The Muş basin is bounded at north with a fault
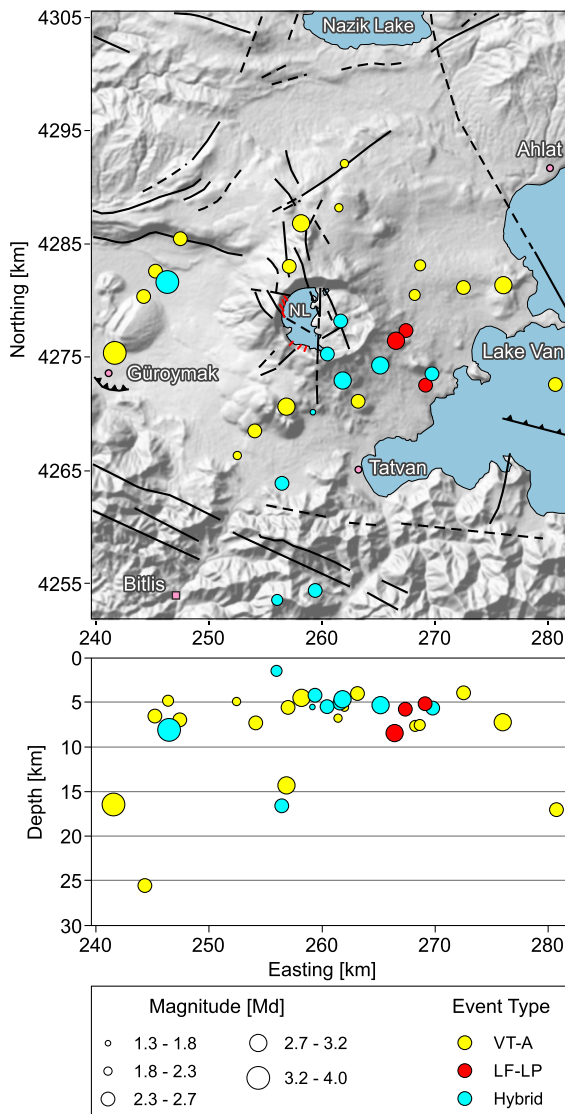
Figure 18

Seismic events of volcanic origin recorded by Hacettepe University Nemrut Monitoring Network around the Nemrut stratovolcano between 2003 and 2005. *VT-A* Volcano-tectonic, *LF-LP* Low frequency-long period. The data were obtained from Ulusoy (2008). The map uses Universal Transverse Mercator projection with WGS 84 datum in 38 Northern Hemisphere Zone

with post-caldera activity and the shallow magma chamber (Çubukçu 2008).

This first detailed geophysical study performed using total field aeromagnetic anomalies provides insights about the inner structures of Nemrut stratovolcano. This study also shows the significance of using appropriate and complementary data processing techniques when dealing with magnetic anomaly maps involving both short- and long-wavelength effects caused by the volcanic rock assemblages.

Publisher's Note   Springer Nature remains neutral with regard to jurisdictional claims in published maps and institutional affiliations.

(Fig. 3) of dextral and strike-slip components (Dhont and Chorowicz 2006). The right lateral (strike-slip) movement of the northern margin of Muş basin with respect to the southern thrust (the Bitlis–Zagros suture zone) would result in localized extension on the northern margin where Nemrut volcano occurs. The existence of an extension regime is associated

REFERENCES

Afshar, A., Norouzi, G. H., Moradzadeh, A., Riahi, M. A., & Porkhial, S. (2017). Curie point depth, geothermal gradient and heat-flow estimation and geothermal anomaly exploration from integrated analysis of aeromagnetic and gravity data on the Sabalan Area, NW Iran. *Pure and Applied Geophysics, 174,* 1133–1152.

Aghajani, H., Moradzadeh, A., & Zeng, H. (2010). Detection of high-potential oil and gas fields using normalized full gradient of gravity anomalies: A case study in the Tabas Basin, Eastern Iran. *Pure and Applied Geophysics, 2011,* 1851–1863.

Arısoy, M. Ö. (2014). Edge detection of aeromagnetic data: A study from the City of Pisidia Antiocheia, Turkey. *Archaeological Prospection, 21,* 293–300.

Ates, A., & Kearey, P. (1993). Deep structure of the East Mendip Hills from gravity, aeromagnetic and seismic reflection data. *Journal of Geological Society, 150,* 1055–1063.

Ates, A., & Kearey, P. (1995). A new method for determining magnetization direction from gravity and magnetic anomalies: Application to the deep structure of the Worcester Graben. *Journal of Geological Society, 152,* 561–566.

Ateş, A., Kearey, P., & Tufan, S. (1999). New gravity and magnetic anomaly maps of Turkey. *Geophysical Journal International, 136,* 499–502.

Ates, A., Sevinc, A., Kadioglu, Y. K., & Kearey, P. (1997). Geophysical investigations of the deep structure of the Aydin—Milas region, southwest Turkey: Evidence for the possible extension of the Hellenic Arc. *Israel Journal of Earth Sciences, 46,* 29–40.

Aydar, E., Gourgaud, A., Ulusoy, İ., Digonnet, F., Labazuy, P., Sen, E., et al. (2003). Morphological analysis of active Mount Nemrut stratovolcano, eastern Turkey: Evidences and possible impact areas of future eruption. *Journal of Volcanology and Geothermal Research, 123,* 301–312.

Aydemir, A. (2009). Tectonic investigation of central Anatolia, Turkey, using geophysical data. *Journal of Applied Geophysics, 68,* 321–334.

Aydin, A. (2007). Interpretation of gravity anomalies with the normalized full gradient (NFG) method and an example. *Pure and Applied Geophysics, 164,* 2329–2344.

Baldwin, R. T., & Langel, R. A. (1993). *Tables and Maps of the DGRF 1985 and IGRF 1990.* France: IAGA Bulletin.

Balkaya, Ç., Ekinci, Y. L., Göktürkler, G., & Turan, S. (2017). 3D non-linear inversion of magnetic anomalies caused by prismatic bodies using differential evolution algorithm. *Journal of Applied Geophysics, 136,* 372–386.

Balkaya, Ç., Göktürkler, G., Erhan, Z., & Ekinci, Y. L. (2012). Exploration for a cave by magnetic and electrical resistivity surveys: Ayvacık Sinkhole Example, Bozdağ İzmir (Western Turkey). *Geophysics, 77,* B135–B146.

Baranov, V., & Naudy, H. (1964). Numerical calculation of the formulate of reduction to the magnetic pole. *Geophysics, 29,* 67–79.

Bektaş, Ö., Büyüksaraç, A., & Rozimant, K. (2013). 3D modelling and structural investigation of the Central Volcanics in Slovakia using magnetic data. *Carpathian Journal of Earth and Environmental Sciences, 8*(4), 27–33.

Bektaş, Ö., Ravat, D., Büyüksaraç, A., Bilim, F., & Ateş, A. (2007). Regional geothermal characterization of East Anatolia from aeromagnetic, heat flow and gravity data. *Pure and Applied Geophysics, 164,* 975–998.

Berezkin, V. M. (1967). Application of the total vertical gradient of gravity for determination of the depths to the sources of gravity anomalies. *Exploration Geophysics, 18,* 69–79.

Berezkin, V. M. (1973). *Application of Gravity Exploration to Reconnaissance of Oil and Gas Reservoir.* Moscow: Nedra Publishing House.

Berezkin, V. M. (1988). *Full Gradient Method in Geophysical Prospecting.* Moscow: Nedra Publishing House.

Bilim, F., Kosaroglu, S., Aydemir, A., & Buyuksarac, A. (2017). Thermal investigation in the Cappodocia Region, Central Anatolia-Turkey, analyzing curie point depth, geothermal gradient, and heat-flow maps from the aeromagnetic data. *Pure and Applied Geophysics, 174,* 4445–4458.

Blakely, R. J. (1988). Curie temperature isotherm analysis and tectonic implications of aeromagnetic data from Nevada. *Journal of Geophysical Research, 93,* 11817–11832.

Blakely, R. J. (1995). *Potential Theory in Gravity and Magnetic Applications.* Cambridge: Cambridge University Press.

Bott, M. H. P. (1960). The use of rapid digital computing methods for direct gravity interpretation of sedimantary basins. *Royal Astronomical Society of Geophysics, 3*(1), 63–67.

Boukerbout, H., Abtout, A., Gibert, D., Henry, B., Bouyahiaoui, B., & Derder, M. E. M. (2018). Identification of deep magnetized structures in the tectonically active Chlef area (Algeria) from

aeromagnetic data using wavelet and ridgelet transforms. *Journal of Applied Geophysics, 154,* 167–181.

Bozkurt, E. (2001). Neotectonics of Turkey—a synthesis. *Geodinamica Acta, 14,* 3–30.

Büyüksaraç, A., Jordanova, D., Ateş, A., & Karloukovski, V. (2005). Interpretation of the gravity and magnetic anomalies of the Cappadocia Region, Central Turkey. *Pure and Applied Geophysics, 162,* 2197–2213.

Cordell, L., & Grauch, V. J. S. (1985). Mapping basement magnetization zones from aeromagnetic data in the San Juan Basin, New Mexico. In W. J. Hinze (Ed.), *The Utility of Regional Gravity and Magnetic Anomaly Maps* (pp. 181–197). Tulsa: Society of Exploration Geophysics.

Cordell, L., & Henderson, R. G. (1968). Iterative three-dimensional solution of gravity anomaly data using a digital computer. *Geophysics, 33*(4), 596–601.

Çubukçu, H. E. (2008). Petrologic evolution of Nemrut Stratovolcano (Turkey): Peralkaline magmatism in a collisional domain. PhD. Thesis, Hacettepe University–Turkey.

Çubukçu, H. E., Ulusoy, İ., Ersoy, O., Aydar, E., Gourgaud, A., & Herve, G. (2012). Mt. Nemrut Volcano (Eastern Turkey): Temporal petrological evolution. *Journal of Volcanology and Geothermal Research, 209–210,* 33–60.

Dhont, D., & Chorowicz, J. (2006). Review of the neotectonics of the Eastern Turkish-Armenian Plateau by geomorphic analysis of digital elevation model imagery. *International Journal of Earth Sciences, 95,* 34–49.

Ekinci, Y. L. (2017). A comparative study on computing horizontal derivatives of gravity data for geological contact mapping. *Geological Bulletin of Turkey, 60*(2), 209–221.

Ekinci, Y. L., Ertekin, C., & Yiğitbaş, E. (2013). On the effectiveness of directional derivative based filters on gravity anomalies for source edge approximation: Synthetic simulations and a case study from the Aegean Graben System (Western Anatolia, Turkey). *Journal of Geophysics and Engineering, 10*(3), 035005.

Ekinci, Y. L., Özyalın, Ş., Sındırgı, P., Balkaya, Ç., & Göktürkler, G. (2017). Inversion of analytic signal amplitude of magnetic data using differential evolution algorithm. *Journal of Geophysics and Engineering, 14,* 1492–1508.

Ekinci, Y. L., & Yiğitbaş, E. (2012). Geophysical approach to the igneous rocks in the Biga Peninsula (NW Turkey) based on airborne magnetic anomalies: Geological implications. *Geodinamica Acta, 25,* 267–285.

Ekinci, Y. L., & Yiğitbaş, E. (2015). Interpretation of gravity anomalies to delineate some structural features of Biga and Gelibolu peninsulas, and their surroundings (north-west Turkey). *Geodinamica Acta, 27,* 300–319.

Elysseieva, I. S., & Pašteka, R. (2019). Review paper: Historical development of the total normalized gradient method in profile gravity field interpretation. *Geophysical Prospecting, 67,* 188–209.

Ercan, T., Matsuda, J. I., Nagao, K., & Kita, I. (1995). Noble gas isotopic compositions in gas and water samples from Anatolia. In: Erler A, Ercan T, Bingöl E, Örçen S (Eds.), Geology of the Black Sea Region: Proceedings of International Symposium on the Geology of the Black Sea Region, Ankara, Turkey, General Directorate of Mineral Research and Exploration and the Chambers of Geological Engineers of Turkey, 197–206.

Fedi, M., Florio, G., & Rapolla, A. (1998). 2.5D modelling of Somma-Vesuvius structure by aeromagnetic data. *Journal of Volcanology and Geothermal Research, 82,* 239–247.

Grant, F. S. (1985). Aeromagnetic, geology and ore environments, I. Magnetite in igneous, sedimentary and metamorphic rocks: An overview. *Geoexploration, 23,* 303–333.

Grauch, V. J. S., & Campbell, D. L. (1984). Does draping aeromagnetic data reduce terrain-induced effects? *Geophysics, 49,* 75–80.

Güleç, N., Hilton, D. R., & Mutlu, H. (2002). Helium isotope variations in Turkey: Relationship to tectonics, volcanism and recent seismic activities. *Chemical Geology, 187,* 129–142.

Güner, Y. (1984). *Doğu Anadolu Kuvaterner volkanizması (Nemrut Yanardağı)* (p. 77). Ankara: MTA Genel Müdürlüğü, Temel Araştırmalar Dairesi.

Hinze, W. J., von Frese, R. R. B., & Saad, A. H. (2013). *Gravity and magnetic exploration: Principles, practices and applications.* Cambridge: Cambridge University Press.

Karakhanian, A., Djrbashian, R., Trifonov, V., Philip, H., Arakelian, S., & Avagian, A. (2002). Holocene-historical volcanism and active faults as natural risk factors for Armenia and adjacent countries. *Journal of Volcanology and Geothermal Research, 113,* 319–344.

Karaoğlu, Ö., Elshaafi, A., Salah, M. K., Browning, J., & Gudmundsson, A. (2017). Large-volume lava flows fed by a deep magmatic reservoir at Ağrı Dağı (Ararat) volcano, Eastern Turkey. *Bulletin of Volcanology, 79,* 15.

Karaoğlu, Ö., Özdemir, Y., & Tolluoğlu, A. Ü. (2004). Physical evolution, emplacement of ignimbrite and characteristic eruption types of Nemrut Stratovolcano: a caldera system at Eastern Anatolia-Turkey. In: Proceedings of the 5th International Symposium on Eastern Mediterranean Geology.

Karaoğlu, Ö., Özdemir, Y., Tolluoğlu, A. Ü., Karabıyıkoğlu, M., Köse, O., & Froger, J. (2005). Stratigraphy of the volcanic products around Nemrut caldera: implications for reconstruction of the caldera formation. *Turkish Journal of Earth Sciences, 14,* 123–143.

Kearey, P. (1991). A possible basaltic deep source of the south-central England magnetic anomaly. *Journal of Geological Society, 148,* 775–780.

Kearey, P., Brooks, M., & Hill, I. (2002). *An introduction to geophysical exploration* (3rd ed.). New Jersey: Blackwell Science Ltd.

Kipfer, R., Aeschbach-Hertig, W., Baur, H., Hofer, M., Imboden, D. M., & Signer, P. (1994). Injection of mantle-type helium into Lake Van (Turkey): the clue for quantifying deep water renewal. *Earth and Planetary Science Letters, 125,* 357–370.

Koçyiğit, A., Yılmaz, A., Adamiac, S., & Kuloshvili, S. (2001). Neotectonics of East Anatolian Plateau (Turkey) and Lesser Caucasus: implication for transition from thrusting to strike-slip faulting. *Geodinamica Acta, 14,* 177–195.

Kurttaş, T., & Tezcan, L. (2018). Nemrut kaldera göllerinin su kaynakları potansiyeli. *Süleyman Demirel University Journal of Natural and Applied Sciences, 22,* 823–831.

Kuzucuoğlu, C., Şengör, A. M. C., & Çiner, A. (2019). The Tectonic Control on the Geomorphological Landscapes of Turkey. In C. Kuzucuoğlu, A. Çiner, & N. Kazancı (Eds.), *Landscapes and landforms of Turkey.* Cham: Springer.

Longo, L. M., De Ritis, R., Ventura, G., & Chiappini, M. (2016). Analysis of the aeromagnetic anomalies of the Auca Mahuida Volcano, Patagonia, Argentina. *Pure and Applied Geophysics, 173,* 3273–3290.

MTA (General Directorate of Mineral Research and Exploration of Turkey), 2010. Airborne regional aeromagnetic anomaly map of Turkey. Ankara: MTA Publications, scale: 1/2000000.

Nagao, K., Matsuda, J. I., Kita, I., & Ercan, T. (1989). Noble gas and carbon isotopic composition in Quaternary volcanic area in Turkey. *Bulletin of Geomorphology, 17,* 101–110.

Nicolosi, I., Caracciolo, F. D., Pignatelli, A., & Chiappini, M. (2019). Imaging the Bracciano caldera system by aeromagnetic data inversion (Sabatini Volcano District, Central Italy). *Journal of Volcanology and Geothermal Research, 388,* 106680.

Okay, A. I., & Tüysüz, O. (1999). Tethyan sutures of northern Turkey. The Mediterranean Basins: Tertiary extension within the Alpine orogen. In: Durand B, Jolivet L, Horváth F, Séranne M (Eds.). *Geological Society of London, 156,* 475–515.

Oruç, B., & Keskinsezer, A. (2008). Detection of causative bodies by normalized full gradient of aeromagnetic anomalies from east Marmara region, NW Turkey. *Journal of Applied Geophysics, 65,* 39–49.

Özdemir, Y., Karaoğlu, Ö., Tolluoğlu, A. Ü., & Güleç, N. (2006). Volcanostratigraphy and petrogenesis of the Nemrut stratovolcano (East Anatolian High Plateau): the most recent post-collisional volcanism in Turkey. *Chemical Geology, 226,* 189–211.

Pamukçu, O., Gönenç, T., Çırmık, A., Pamukçu, Ç., & Ertürk, N. (2019). Geothermal potential of Büyük Menderes Graben obtained by combined 2.5 D normalized full gradient results. *Pure and Applied Geophysics, 176,* 5003–5026.

Paoletti, V., Fedi, M., & Florio, G. (2017). The structure of the Ischia Volcanic Island from magnetic and gravity data. *Annals of Geophysics, 60,* GM674.

Pašteka, R. (2000). 2D semi-automated and environmental methods in gravimetry and magnetometry. *Acta Geologica Universitatis Comenianae, 55,* 5–50.

Patella, D., & Mauriello, P. (1999). The geophysical contribution to the safeguard of historical sites in active volcanic areas. The Vesuvius case-history. *Journal of Applied Geophysics, 41,* 241–258.

Pilkington, M., & Hildebrand, A. R. (2000). Three-dimensional magnetic imaging of the Chicxulub Crater. *Journal of Geophysical Research, 105,* 23479–23491.

Quarta, T., Fedi, M., & De Santis, A. (2000). Source ambiguity from an estimation of the scaling exponent of potential field power spectra. *Geophysical Journal International, 140,* 311–323.

Reynolds, J. M. (1997). *An Introduction to applied and environmental geophysics.* Chichester: Wiley.

Sawires, R., & Aboud, E. (2019). Subsurface structural imaging of Ceboruco Volcano area, Nayarit, Mexico using high-resolution aeromagnetic data. *Journal of Volcanology and Geothermal Research, 371,* 162–176.

Secomandi, M., Paoletti, V., Aiello, G., Fedi, M., Marsela, E., Ruggieri, S., et al. (2003). Analysis of the magnetic anomaly field of the volcanic district of the Bay of Naples, Italy. *Marine Geophysical Researches, 24,* 207–221.

Şen, P. A., Temel, A., & Gourgaud, A. (2004). Petrogenetic modeling of Quaternary post-collisional volcanism: a case study of central and eastern Anatolia. *Geological Magazine, 141,* 81–98.

Şengör, A. M. C., Görür, N., & Şaroğlu, F. (1985). Strike-slip Faulting and Related Basin Formation in Zones of Tectonic

Escape: Turkey as a Case Study. In K. T. Biddle & N. Christie-Blick (Eds.), *Strike-slip deformation, Basin formation, and sedimentation*. Texas: SEPM Society for Sedimentary Geology Publications.

Şengör, A. M. C., Özeren, M. S., Keskin, M., Sakınç, M., Özbakır, A. D., & Kayan, İ. (2008). Eastern Turkish high plateau as a small Turkic-type orogen: Implications for post-collisional crust-forming processes in Turkic-type orogens. *Earth-Science Reviews, 90,* 1–48.

Şengör, A. M. C., & Yılmaz, Y. (1981). Tethyan evolution of Turkey: A plate tectonic approach. *Tectonophysics, 75,* 181–241.

Şerefhan (1597). *Şerefname: Kürt tarihi (translated from Arabic to Turkish by M. Emin Bozarslan, 1971)*. İstanbul: Ant Press.

Seven, E., Mironov, V., & Akın, K. (2019). A new species of *Eupithecia* Curtis (Lepidoptera: Geometridae, Larentiinae). *Zootaxa, 4668,* 443–447.

Sharma, P. V. (1986). *Geophysical methods in geology* (2nd ed.). New York: Elsevier Science.

Sheng, Z., & Xiaohong, M. (2015). Improved normalized full-gradient method and its application to the location of source body. *Journal of Applied Geophysics, 113,* 86–91.

Sındırgı, P., & Özyalın, Ş. (2019). Estimating the location of a causative body from a self-potential anomaly using 2D and 3D normalized full gradient and Euler deconvolution. *Turkish Journal of Earth Sciences, 28,* 640–659.

Sındırgı, P., Pamukçu, O., & Özyalın, Ş. (2008). Application of normalized full gradient method to self potential (SP) data. *Pure and Applied Geophysics, 165,* 409–427.

Soleimani, M., Aghajani, H., & Heydarinejad, S. (2018). Salt dome boundary detection in seismic image via resolution enhancement by the improved NFG method. *Acta Geodaetica et Geophysica, 53,* 463–478.

Spector, A., & Grant, F. S. (1970). Statistical models for interpreting aeromagnetic data. *Geophysics, 35,* 293–302.

Szitkar, F., & Dyment, J. (2015). Near-seafloor magnetics reveal tectonic rotation and deep structure at the TAG (Trans-Atlantic Geotraverse) hydrothermal site (Mid-Atlantic Ridge, 20°N). *Geology, 43,* 87–90.

Szitkar, F., Petersen, S., Tontini, F. C., & Cocchi, L. (2015). High-resolution magnetics reveal the deep structure of a volcanic-arc-related basalt-hosted hydrothermal site (Palinuro, Tyrrhenian Sea). *Geochemistry, Geophysics, Geosystems, 16,* 1950–1961.

Telford, W. M., Geldart, L. P., Sheriff, R. E., & Keys, D. A. (1990). *Applied geophysics* (2nd ed.). Cambridge: Cambridge University Press.

Tivey, M. A., & Dyment, J. (2010). The Magnetic Signature of Hydrothermal Systems in Slow Spreading Environments. In P. A. Rona, C. W. Devey, J. Dyment, & B. J. Murton (Eds.), *Diversity of Hydrothermal Systems on Slow Spreading Ocean Ridges*. Florida: American Geophysical Union Publishing.

Tivey, M. A., Rona, P. A., & Schouten, H. (1993). Reduced crustal magnetization beneath the active mound, TAG hydrothermal field, Mid-Atlantic Ridge, at 26°N. *Earth and Planetary Science Letters, 115,* 101–115.

Ulusoy, İ. (2008). Etude volcano-structurale du volcan Nemrut (Anatolie de l'Est Turquie) et risques naturels associés. PhD. Thesis, University of Clermont-Ferrand II, France & Hacettepe University, Turkey.

Ulusoy, İ., Çubukçu, H. E., Aydar, E., Labazuy, P., Ersoy, O., Şen, E., et al. (2012). Volcanological evolution and caldera forming eruptions of Mt. Nemrut (Eastern Turkey). *Journal of Volcanology and Geothermal Research, 245–246,* 21–39.

Ulusoy, İ., Çubukçu, H. E., Mouralis, D., & Aydar, E. (2019). Nemrut Caldera and Eastern Anatolian Volcanoes: Fire in the Highlands. In: Ed. Kuzucuoğlu, C., Çiner, A., Kazancı, N. Landscapes and Landforms of Turkey, Springer International Publishing, New York. pp 589–599.

Ulusoy, İ., Labazuy, P., Aydar, E., Ersoy, O., & Çubukçu, E. (2008). Structure of the Nemrut caldera (Eastern Anatolia, Turkey) and associated hydrothermal fluid circulation. *Journal of Volcanology and Geothermal Research, 174,* 269–283.

USGS, (2010). Porphyry copper assessment of the Tethys Region of Western and Southern Asia. Scientific Investigation Report, 2010–5090–V.

Walls, C. C., & Hall, J. M. (1998). Interpretation of aeromagnetic anomalies in terms of hydrothermal alteration in Cretaceous normal polarity superchron extrusives of the Troodos, Cyprus, ophiolite. *Journal of Geophysical Research, 103,* 30311–30321.

Wessel, P., & Smith, W. H. F. (1995). New version of the Generic Mapping Tools. *Eos Transactions, American Geophysical Union, 76,* 329.

Xu, Y., Hao, T., Zhao, B., Lihong, Z., Zhang, L., Li, Z., et al. (2011). Investigation of igneous rocks in Huanghua depression, North China, from magnetic derivative methods. *Journal of Geophysics and Engineering, 8,* 74–82.

Yiğitbaş, E., Elmas, A., Sefunç, A., & Özer, N. (2004). Major neotectonic features of eastern Marmara region, Turkey: Development of the Adapazari-Karasu corridor and its tectonic significance. *Geological Journal, 39,* 179–198.

Yılmaz, Y., Güner, Y., & Şaroğlu, F. (1998). Geology of the Quaternary volcanic centres of the east Anatolia. *Journal of Volcanology and Geothermal Research, 85,* 173–210.

Yılmaz, Y., Şaroğlu, F., & Güner, Y. (1987). Initiation of the neomagmatism in East Anatolia. *Tectonophsics, 137,* 177–199.

Zeng, H., Meng, X., Yao, C., Li, X., Lou, H., Guang, Z., et al. (2002). Detection of reservoirs from normalized full gradient of gravity anomalies and its application to Shengli oil field, east China. *Geophysics, 67,* 1138–1147.

Zeng, H., Xu, D., & Tan, H. (2007). A model study for estimating optimum upward -continuation height for gravity separation with application to a Bouguer gravity anomaly over a mineral deposit, Jilin province, northeast China. *Geophysics, 72,* I45–I50.

Zurek, J., & Williams-Jones, G. (2013). The shallow structure of Kilauea caldera from high-resolution Bouguer gravity and total magnetic anomaly mapping: insights into progressive magma reservoir growth. *Journal of Geophysical Research: Solid Earth, 118,* 3742–3752.